International Journal of
Physical Sciences

Science

academicJournals

Academic
Journals

ABOUT IJPS

The **International Journal of Physical Sciences (IJPS)** is published weekly (one volume per year) by Academic Journals.

International Journal of Physical Sciences (IJPS) is an open access journal that publishes high-quality solicited and unsolicited articles, in English, in all Physics and chemistry including artificial intelligence, neural processing, nuclear and particle physics, geophysics, physics in medicine and biology, plasma physics, semiconductor science and technology, wireless and optical communications, materials science, energy and fuels, environmental science and technology, combinatorial chemistry, natural products, molecular therapeutics, geochemistry, cement and concrete research, metallurgy, crystallography and computer-aided materials design. All articles published in IJPS are peer-reviewed.

Contact Us

International Journal of Physical Sciences

Table of Contents: Volume 13   Number 4,   28 February, 2018

ARTICLES

Full Length Research Paper

Interpretation of aeromagnetic data over some parts of Mambilla Plateau, Taraba State

YAKUBU John Akor*, ILEAGU Immaculate Ukamaka and IGWE Emmanuel Awucha

Department of Physics and Astronomy, University of Nigeria, Nsukka, Nigeria.

The data covering Mayo Daga and Gashaka areas of Taraba State has been interpreted by applying source parameter imaging (SPI) and forward and inverse modeling methods. From the quantitative method of interpretation, it was found out that the magnetic intensity within the study area ranges from -129.9 to 186.6 nT in which the area is noticeably marked by both low and high magnetic signatures which may be as a result of several factors such as; susceptibility, degree of strike, difference in magnetic variation in depth and difference in lithology. From the quantitative interpretation, depth estimates obtained when SPI is employed shown minimum to maximum depth to anomalous source that ranges from 400.7 to 2119.2 m. Forward and inverse modeling estimated depths for profiles P1, P2, P3, and P4 were 2372, 2537, 1621 and 1586 m, respectively, with susceptibility values of 0.0754, 0.0251, 0.0028, and 0.001 respectively, suggesting that the bodies causing the anomaly are typical of igneous rocks; basalt and olivine, intermediate igneous rock; granites, and rocks mineral (quartz).

Key words: Aeromagnetic data, source parameter imaging (SPI), qualitative and quantitative interpretation

INTRODUCTION

Minerals and hydrocarbon play vital roles in the socio-economic development of a country of which Nigeria is not an exception. Aeromagnetic surveys are widely used to aid production of geological maps, regional geological studies, location and definition of buried metallic objects, engineering site investigation, archeo-geophysics and are also commonly used for mineral exploration by detecting minerals or rocks with unusual magnetic properties which reveal themselves by causing anomalies in the magnetic field intensity of the earth. Aeromagnetic maps usually show changes in the earth's magnetic field resulting from the properties of rock sediments (e.g. magnetic

susceptibilities). Basic igneous rocks have the highest magnetic susceptibility, while acidic igneous rocks have intermediate magnetic susceptibility and sedimentary rocks have the lowest magnetic (Kearey et al., 2002). Some minerals deposits are associated with abundance of magnetic minerals, and occasionally the target may itself be magnetic (e.g. iron ore deposits), but often the elucidation of surface structure of the upper crust is the most valuable contribution of the aeromagnetic data (Hamza and Garba, 2010). This method plays a distinguished role when compared with other geophysical methods, it is cheaper, faster and large area of land

*Corresponding author. E-mail: john.yakubu@unn.edu.ng.
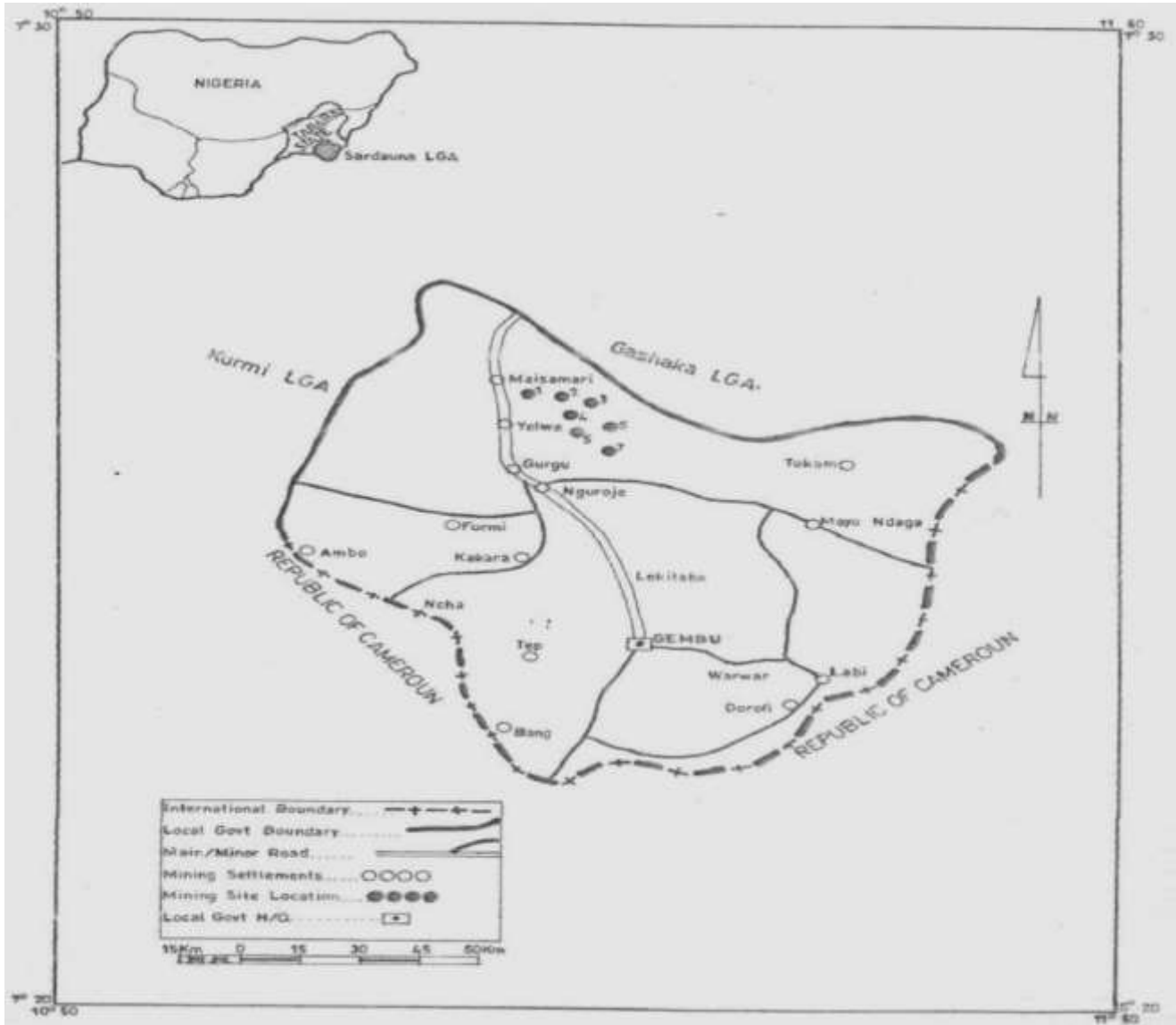
Figure 1. Map of Nigeria showing the study area.
Source: Ahmed and Oruonye (2016).

especially areas of political barrier, economic, social and environmentally hazardous can easily be covered. The main purpose of this work is to study the magnetic anomalies of Mayo Daga and Gashaka areas, by interpreting qualitatively and quantitatively the aeromagnetic anomaly of the areas. The purposes are; to estimate the basement depth, to determine the magnetic susceptibility and type of mineralization prevalent in the area.

Location and geology of the study area

The study area is located in Mambilla Plateau, Sardauna

Local Government Area of Taraba State. It is located between latitude 5°30' to 7°18' and longitude 10°18' to 11°37' having a total land mass of 3,765.2 km^2 and forms the southernmost tip of east of northern part of Nigeria (Tukur et al., 2005). This plateau is Cameroon-locked in the southern, eastern and western part as shown in Figure 1 (Frantz, 1981).

According to Mubi and Tukur (2005), the basement complex rocks underlay more than two-third of the plateau and dates back to the Precambrian to early Paleozoic era. Meanwhile, according to Jeje (1983), the remaining part of the plateau is made up of volcanic rocks of the upper Cenozoic to tertiary and quaternary ages. These rocks found within the plateau are of

volcanic origin, extended from tectonic lines, fissures, etc. These volcanic rocks comprises olivine basalt, basalts suite and trachyte basalt which were found to contain mixtures of amphiboles, pyroxenes with some other free minerals of quartz (Mould, 1960). The tertiary basalts are found in the Mambilla Plateau mostly formed by trachytic lavas and extensive basalts (Dupreez and Barber, 1995).

DATA SOURCE AND METHODOLOGY

The data covering the study area was obtained from Nigeria Geological Survey Agency (NGSA). The company, FURGRO Airborne Surveys in collaboration with Federal Government of Nigeria and World Bank carried out the acquisition and processing of data with a terrain clearance of 100 m, altitude of 80 m, 100 m flight line spacing and 500 m tie line spacing. The data obtained from NGSA is in digitized form, XYZ format.

The first stage of interpretation is gridding; it is a process of interpolating data unto an equally spaced grid of cells in a specified coordinate system. Because the XYZ data were collected over widely separated parallel lines which may have resulted in some points along the survey not sampled, it is important that we represent the sampled data by determining the values at points equally spaced far apart at the nodes of a grid.

To produce the grids, "minimum curvature" method was used (Briggs, 1974). This method, also called the random gridding method, fit a minimum curvature surface to data points. The method was used because the data were sparely sampled over wide area and continuous between data points. The RANGRID GX of the Oasis Montaj software was used to achieve this. Here, a grid size of 300 m was used to avoid over or under sampling based on the sampling distance of the data.

The quantitative interpretation of the aeromagnetic data of the study area was carried out by inspecting the TMI gridded map. This map is in colour aggregate, and the general purpose is to gain some preliminary information of source of anomalies (Obiora et al., 2016). Oasis Montaj software was employed in producing the total intensity (TMI) map. From the map, one can talk of certain features about the magnetic intensity and the factors (such as susceptibility, depth to the magnetic bodies, nature of the bodies, etc) responsible for the change in magnetic signatures.

The regional anomaly was separated from the residual anomaly by applying first order polynomial which was fitted by least square method to the data. Different orders of polynomial were tried and it was found that the first order polynomial fitting was the best for our data as it reflected the geological information of the area. The equation used to generate the algorithm for removal of regional data according to Ugwu et al. (2013) is given as:

$$r = a_0 + a_1(X - X_{ref)} + a_2(Y - Y_{ref})$$ (1)

where r is the regional field, X_{ref} and Y_{ref} are the X and Y coordinates of the geographical centre of the dataset respectively. And a_0, a_1 and a_2 are the regional polynomial coefficients.

Quantitative interpretation of aeromagnetic data involves making numerical estimates of dimensions and depth of the anomalies and often takes the form of sources' modelling theoretically replicating the recorded anomalies during the survey. In order to see whether the earth model is consistent with what has been observed, that is, developing a model that is suitable in terms of physical approximation to the unknown geology, conceptual models of the subsurface are created and its anomalies calculated. Quantitatively, forward and inverse modelling and source parameter imaging (SPI) was employed in this research work.

Forward modelling involves comparing of the calculated field with observed data, in which the models are adjusted to improve the fitting of the calculated and observed data. In comparing the calculated field of a hypothetical source with that of the observed data, the model is adjusted in order to improve the fit for a subsequent comparison. This technique makes use of trial and error approach to estimate the distribution of magnetization within the source or geometry of the source. The model may be two- or three- dimensional. In inverse modelling method, some source parameters are determined directly from the measured data which is an opposition to the trial and error or indirect determination. It is customary in this method to constrain some parameters of the source in the way, keeping in mind that every anomaly has an infinite number of permissible sources bringing about infinite number of solutions (Obiora et al., 2016).

The inversion of magnetic data may involve one of the following three approaches; Calculation of depth to source or depth to bottom of source, calculation of magnetic distribution given the geometry of the source and calculation of source geometry given the distribution of magnetization.

Oasis Montaj containing the Potent software was used in the modelling and inversion of the anomalies in this research work. Potent software is a program used for the modelling of the gravitational and magnetic effects of surface and is well suited for modelling ore body in detail for mineral exploration and providing a highly 3-D interactive environment among other applications. In Potent, the main concept includes; calculation, observation, inversion, model and visualisation and the model consist of an assemblage of simple geometrical bodies. Using Potent, the following geometrical bodies can be created; sphere, rectangular prism, cylinder, dyke, lens, slab, ellipsoid and polygonal prism. By trial and error approach, these bodies were attempted in modelling the observed data in order to obtain the best fit model. The observed data were best modelled by sphere, dyke, slab and rectangular prism. In trying to model the observed data of the study area, Potent assigns the body default parameters (physical properties, shapes, position). The body created is modelled by varying any of the parameters of the body. In interpreting the observed data, the first step was to take profiles on the field image. In view of this, seven profiles (P1, P2, P3, P4, P5, P6 and P7) were taken at different parts of the field image. The second quantitative method employed was SPI. Estimation of source parameters can be performed on gridded aeromagnetic data. This has two advantages; 1) it eliminates errors caused by the lines of survey that are not perpendicularly oriented to the strike and secondly, it has no dependency on an operator size or user selected window other techniques like Euler methods and Naudy (1970) requires. Furthermore, output quantities grids can be generated and subsequently, image can be processed to enhance detail of structural information that otherwise may not be evident (Abbas and Mallam, 2013).

This SPI method utilizes the relationship between the local wave number (k) and the source depth of the observed field, for which calculation of any point within a grid of data through vertical and horizontal gradients can be carried out (Thurston and Smith, 1997). According to Thurston and Smith (1997), the original SPI works only for two models: a sloping contact and a dipping thin dike. The maxima of the local wave number (k) is located above isolated contacts and estimate of depths can be made without assumptions about the thickness of the source of bodies. Using SPI method, grids solutions show the edge location, susceptibility contrast, dips and depths. This method requires first and second order derivatives thus making it susceptible to both interference effects and noise in the data (Abbas and Mallam, 2013).

The basics of this method, is that for vertical contacts, the peaks of the k defines the inverse of the depth. Given as;

$$\text{Depth} = \frac{1}{K_{max}} = \frac{1}{(\sqrt{(\delta Tilt/\delta x)^2 + ((\delta Tilt/\delta y)^2)})_{max}}$$ (2)
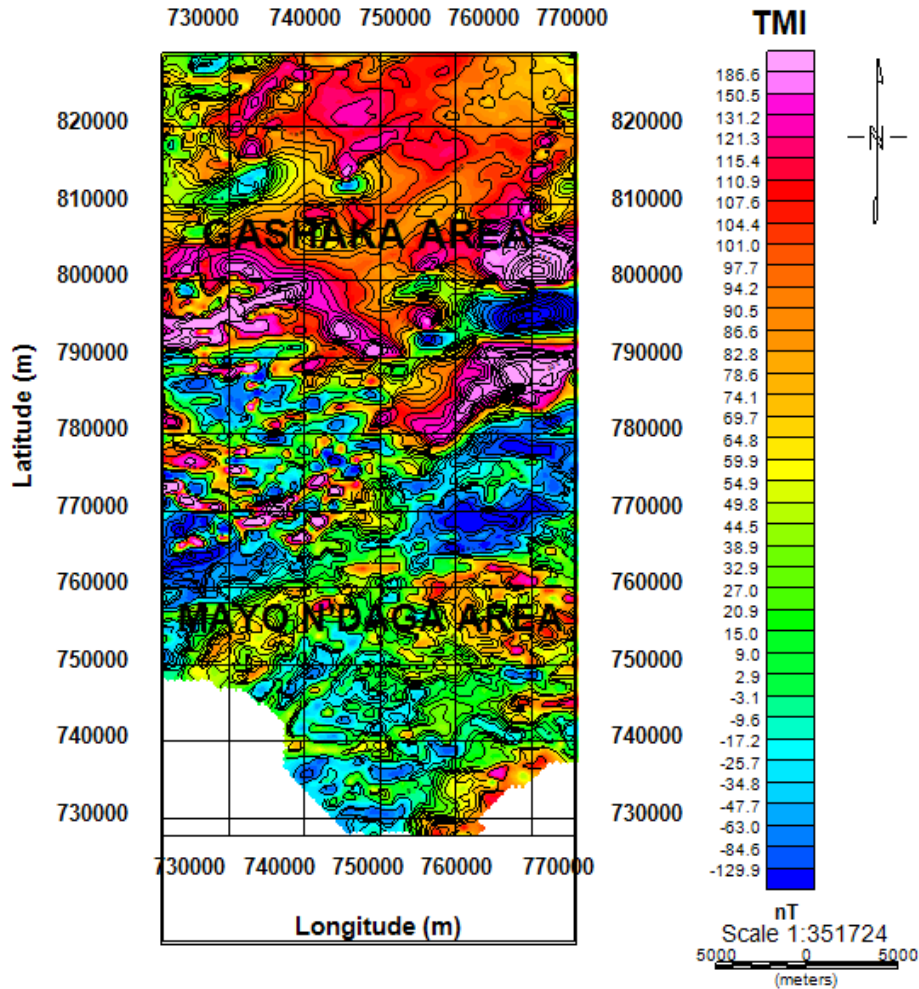
Figure 2. Total magnetic intensity map of the study area.

Where the tilt is given as

$$\text{Tilt} = \arctan\left(\frac{\delta T / \delta z}{(\sqrt{(\delta T / \delta x)^2 + ((\delta T / \delta y)^2})}\right) \tag{3}$$

$$\text{Tilt} = \frac{\delta T / \delta z}{HGRAD} \tag{4}$$

HGRAD =horizontal gradient, T = total magnetic intensity (TMI).

The SPI method helps in calculating the parameters of source from gridded magnetic data. This method assumes either a 2D dipping thin-sheet model or a 2D slopping contact that is based on the complex analytical signal. The solution grids show the dips, depth, susceptibility contrast and the edge location. The depth estimate is not dependent on magnetic declination, inclination, dip, strike or any remanent magnetization. Processing of the SPI image grids provides and enhances maps that facilitate interpretation by non-specialists (Ojoh, 1992).

RESULTS PRESENTATION AND DISCUSSION

Interpreting the data quantitatively, the data was gridded

to produce the total magnetic intensity (TMI) map of the study area which is in colour aggregate (Figure 2). From the TMI map, the magnetic intensity varies between a minimum value of -129.9 nT to a maximum value of 186.6 nT and is marked by both high and low magnetic signatures. These variations may be due to several factors such as; difference in lithology, magnetic susceptibility, variation in degree of strike, depth and difference in lithology. In the northern and southern part of the study area, orientation of the contours is closely spaced. This suggests that local fracture zones or faults may possibly pass via these areas. The elliptically closed contours in the study area equally suggests the presence of magnetic bodies. Most of the anomalous features are trending in the East-western direction. The regional map was separated from the TMI grid to obtain the residual as shown in Figure 3, and ranges from -145.1 to 129.1 with variations in colour as indicated on the legend bar.

In computing the SPI depth, Oasis Montaj software and the generated SPI grid image and legend are employed. Figure 4 shows different colours which is an indication of
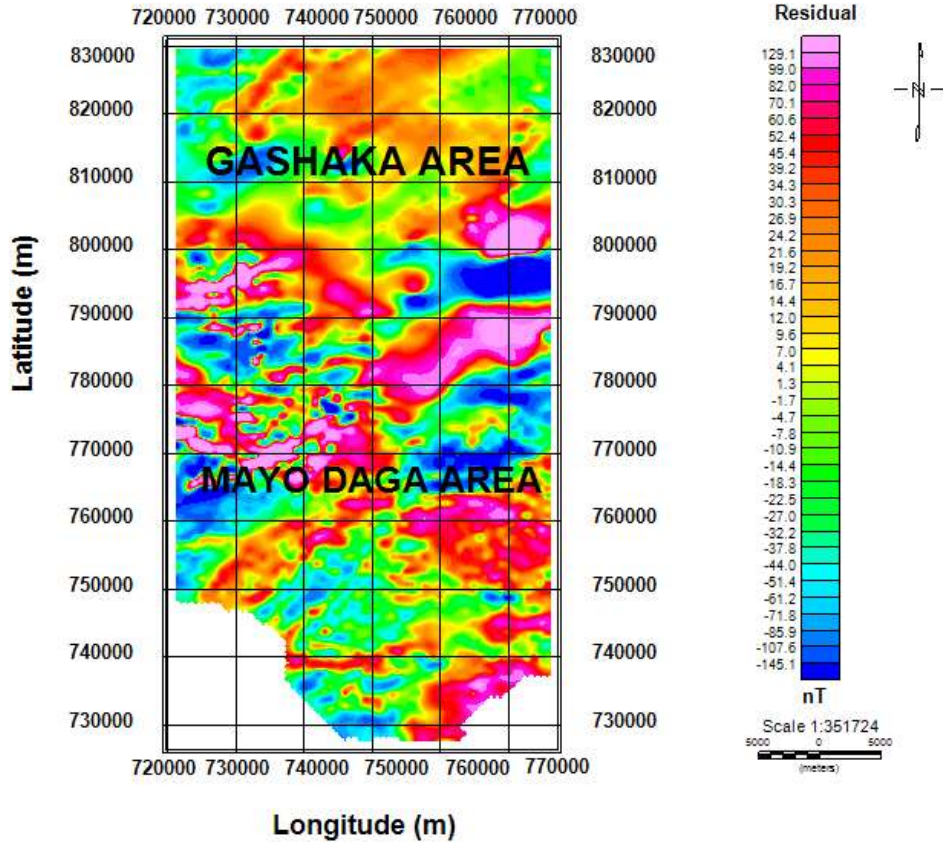
Figure 3. Residual map of the area.
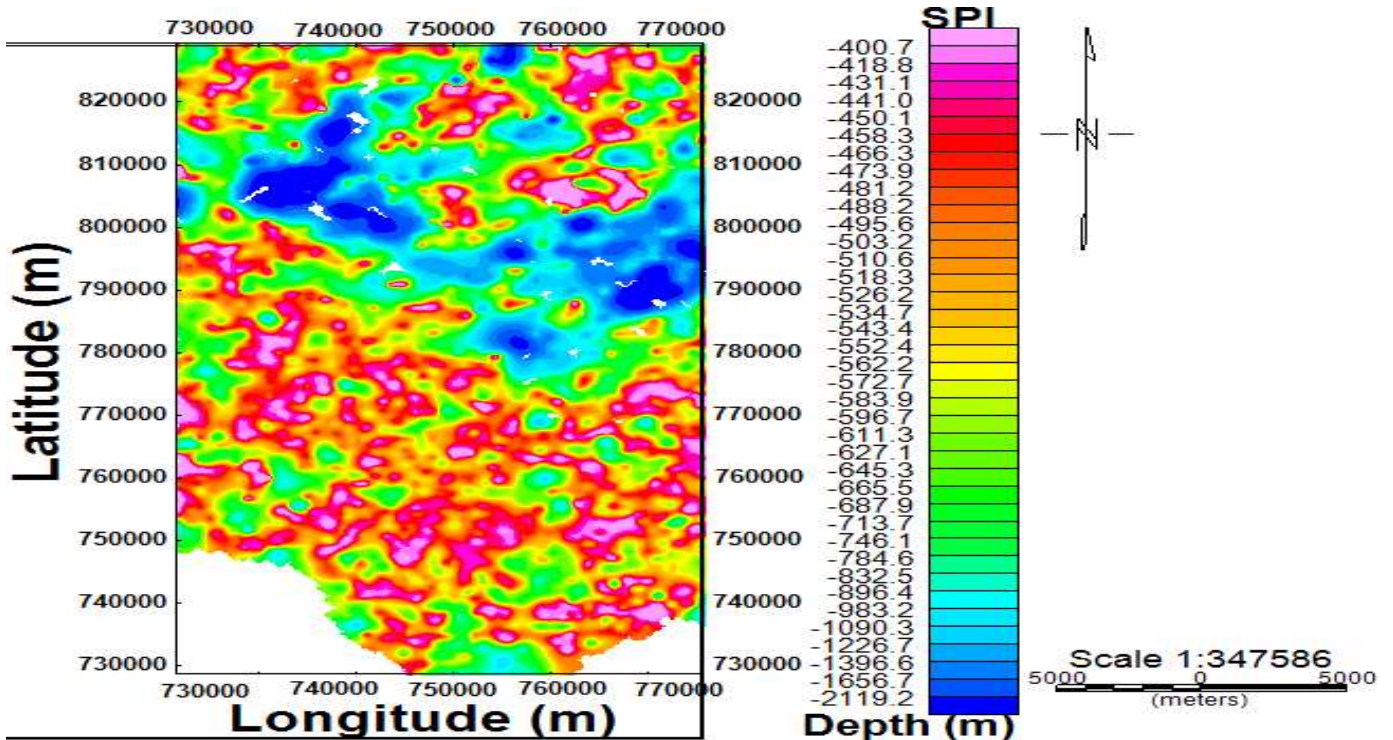
Figure 4. 2-D source parameter imaging (SPI) grid and legends of the study area.
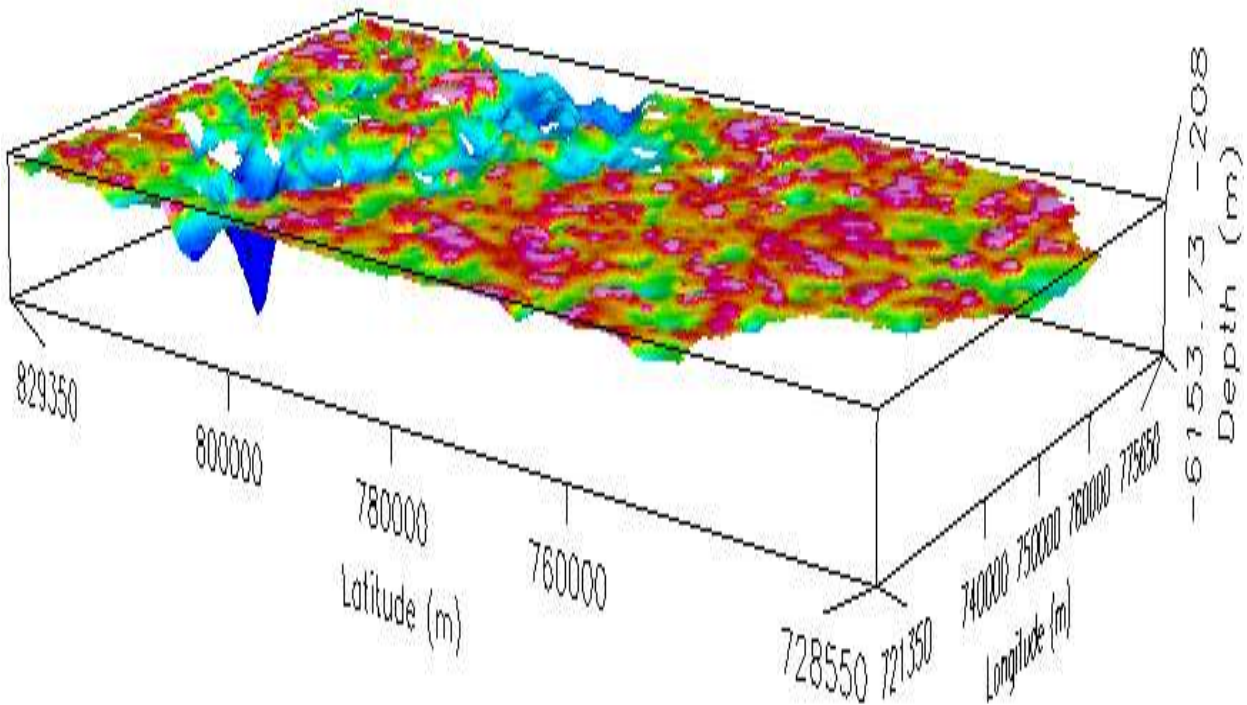
Figure 5. 3-D source parameter imaging (SPI) grid and legends of the study.

varying magnetic susceptibility contrast within the study area and could equally portray the basement surface undulations. Oasis Montaj software was used in computing the SPI image and depth. The generated SPI grid image and SPI legends (Figure 4) show varied colours supposedly indicating different magnetic susceptibility contrasts within the study area, and could also portray the undulations in the basement surface. The negative sign on the legend signifies depth below the subsurface. The blue colour on the map as indicated by the legend shows areas of deep lying or thicker sediments. The pink, purple yellow and orange colours as indicated by the legend show areas of near surface or shallow sediments. The depth to the magnetic source ranges from 400.7 to 2119.2 m as shown in Figure 4. The SPI 3-D view (Figure 5) of the study area in different tilt positions was also shown which showed two main magnetic anomaly source depths indicated by the long spikes (blue colour) representing area having deep lying magnetic bodies hence, with thicker sedimentary cover; and short spikes (light green and orange colours) representing areas of shallow sediment.

To interpret the observed data, four different profiles were taken at different points of the field image. Figure 6 shows the four profiles taken on residual magnetic map of the area of study and the subsets are shown in Figures 7 to 10.

Figures 7 to 10 shows the model profiles of the study area. In the result, the red curves represents the calculated field while the blue colour curves represents the observed field. The shape, physical properties and position were adjusted during the forward modelling session in order to obtain a good correlation between the observed and calculated field. Potent was used to calculate the field at the actual observation points (the points where the observed field is known). The field from the model was automatically calculated in response to the changes made to the model. The observed values are shown as an image and as a single E-W and N-S profile. Their fit is measured by their visible superposition and the root mean square (RMS) values. The root mean square (RMS) difference between the calculated and observed values was minimized by the inversion algorithm. At the end of each inversion exercise, the RMS value was displayed. The RMS value of less than twenty-one (21) was set as a standard for the inversion result as the fit between the observed and calculated field; thereafter, the RMS value was displayed at the end of each inversion exercise. As the fit between observed and calculated field continues to improve, the value of RMS continue decreasing until a reasonable inversion result was achieved.

The sub profiles in each model show the variations of the field values with distance at the area or points modelled. Profiles P1 and P2 taken around north-western and north-eastern parts of the study area were modeled by cylinder shapes emplaced at depths of 2372 and 2537 m respectively (Figures 8 and 9). The bodies have
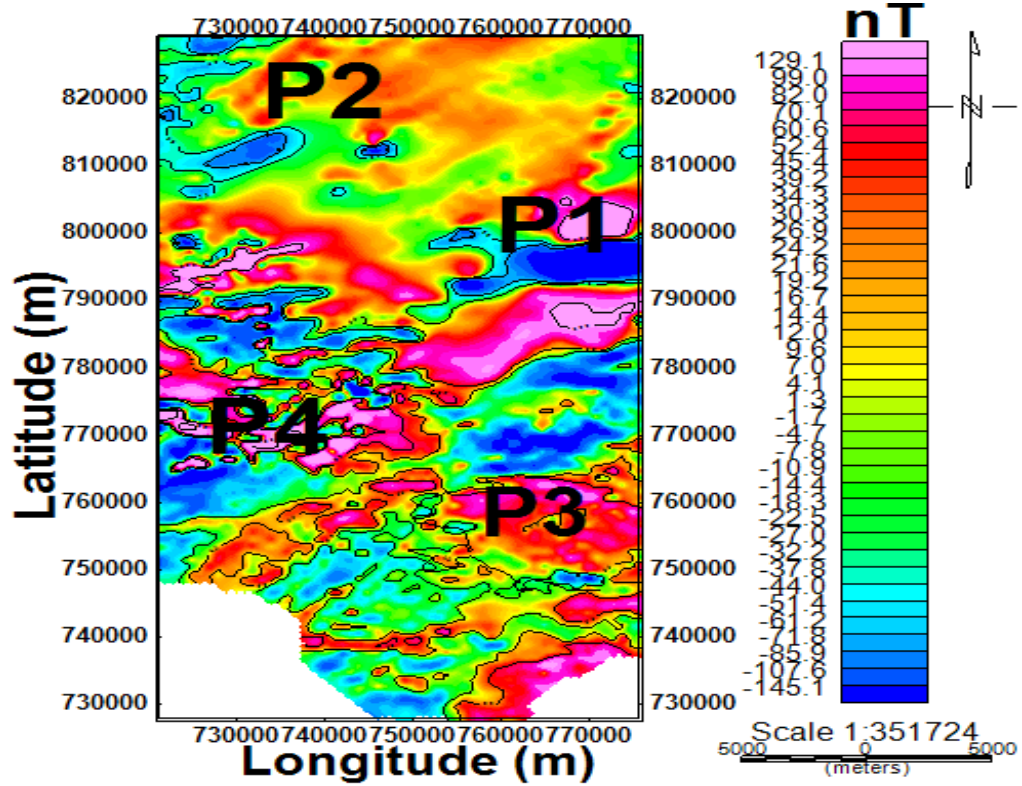
Figure 6. Residual magnetic contour grid map showing four profiles.
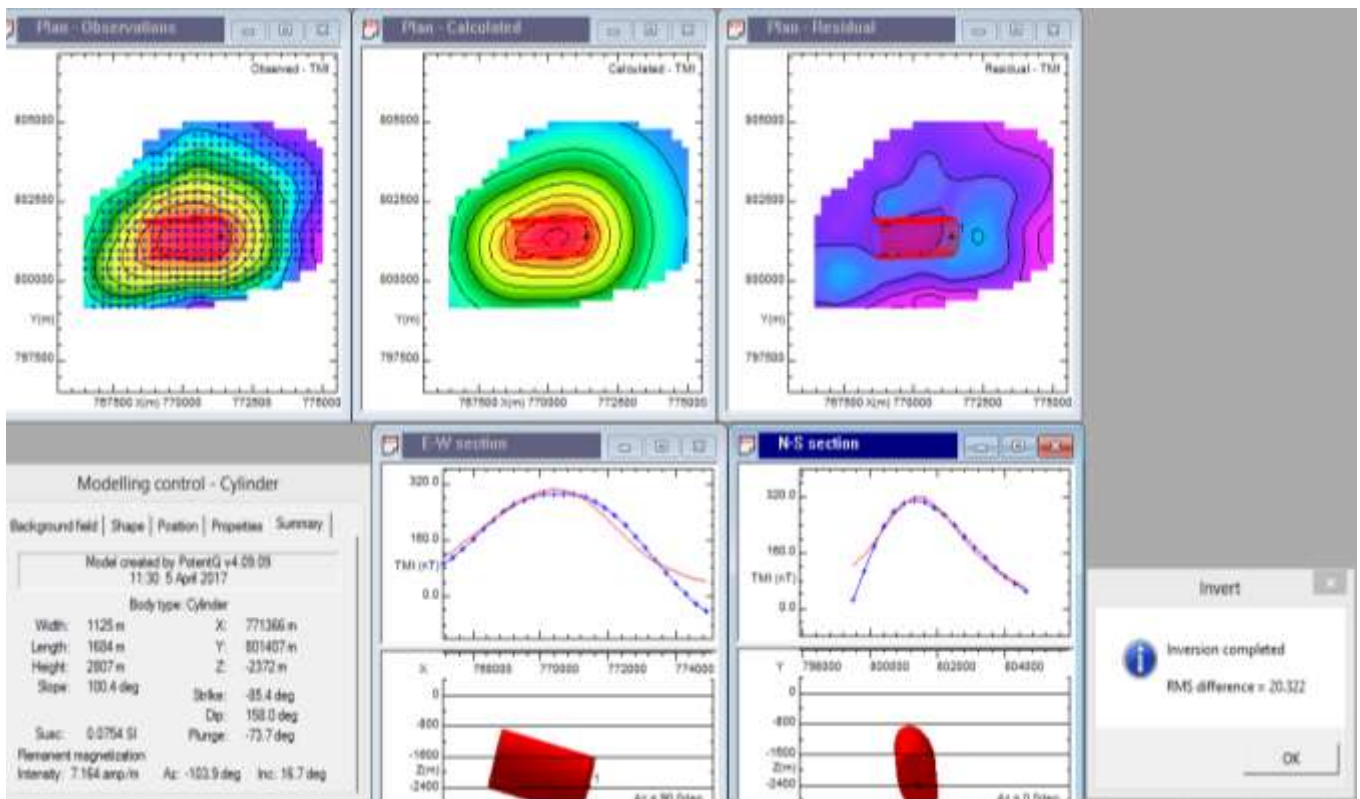
Figure 7. Model (Cylinder) result of profile 1.
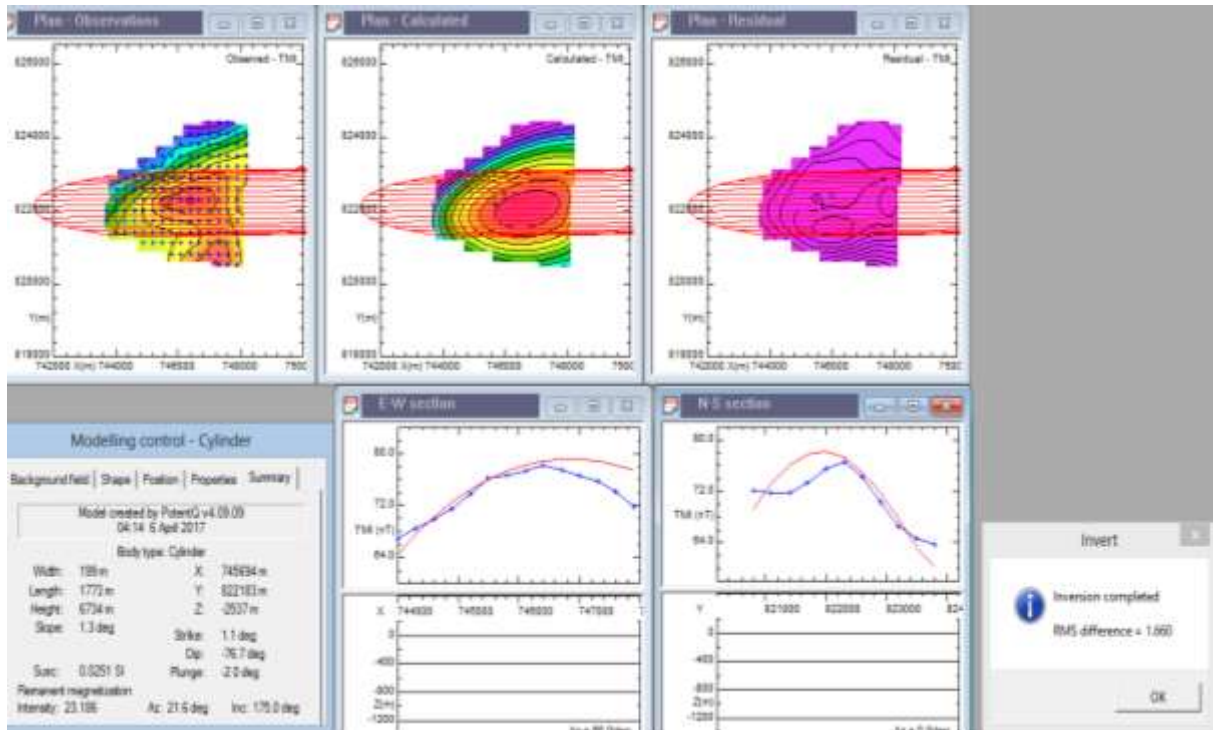
Figure 8. Model (Cylinder) result of profile 2.
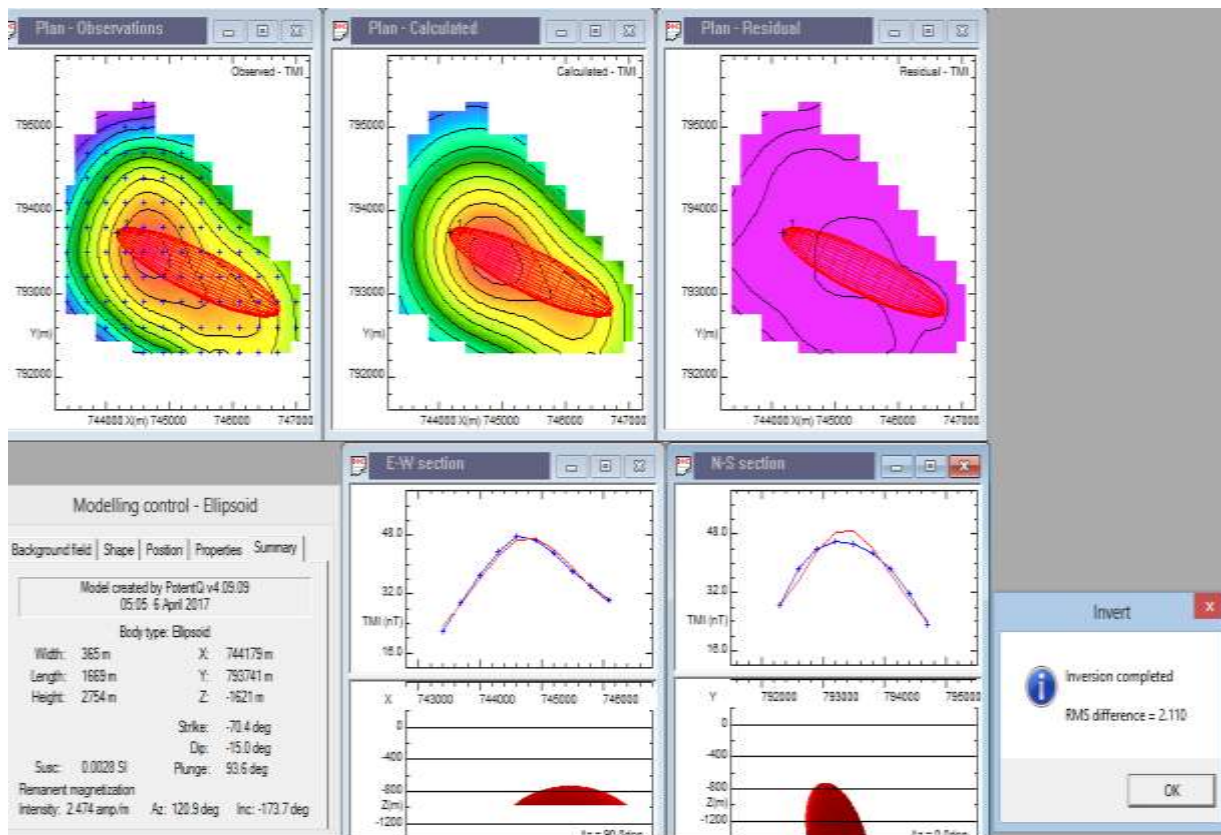
Figure 9. Model (Ellipsoid) result of profile 3.
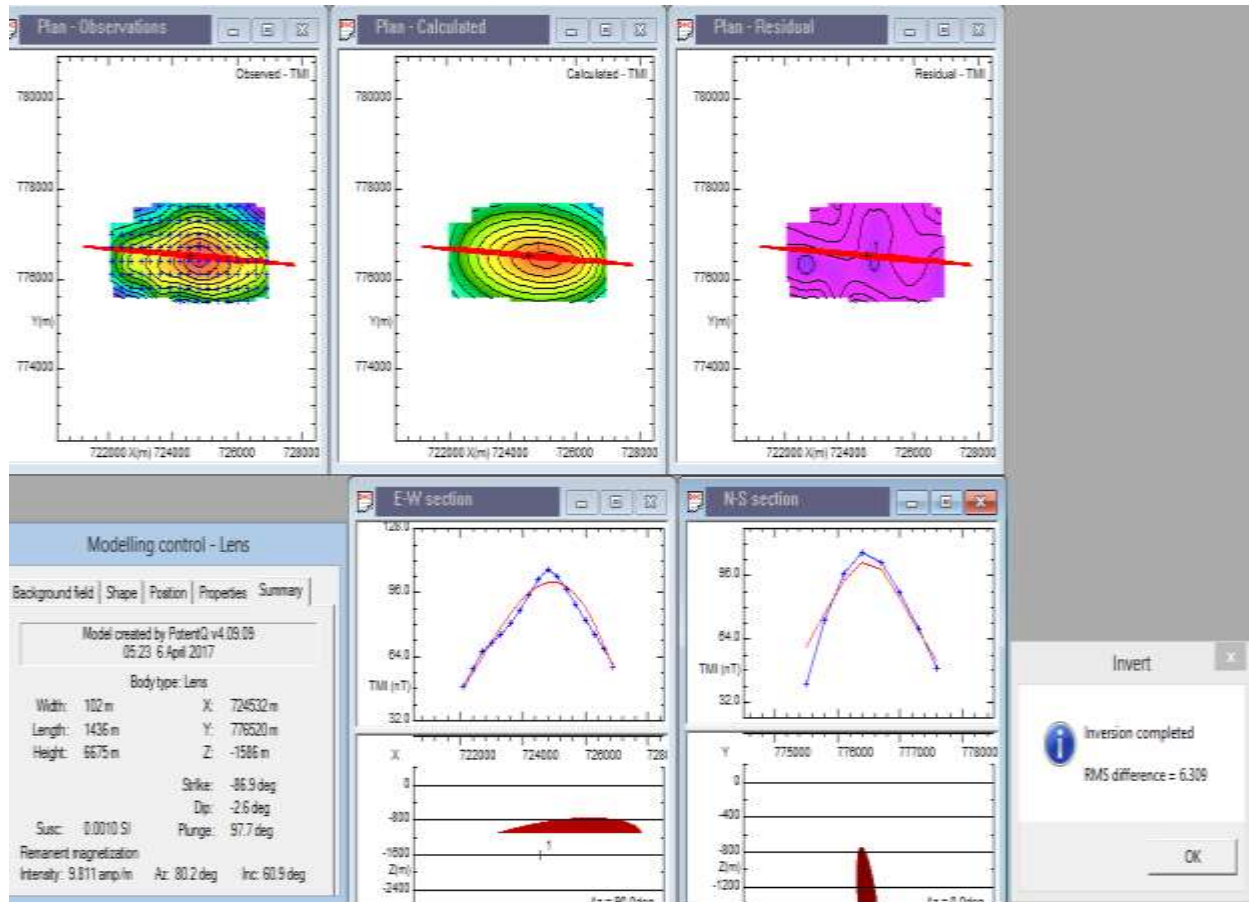
Figure 10. Model (Lens) result of profile 4.

Table 1. Summary of modeling results.

Profile	X(m)	Y(m)	Depth (m)	Types of body	Dip (degree)	Plunge (degree)	Strike (degree)	K value	Possible cause of anomaly
1	771366	801407	-2372	Cylinder	158.0	-73.7	-85.4	0.0754	Basalt
2	745694	822183	-2537	Cylinder	-76.7	-3.0	1.1	0.0251	Olivine
3	744179	793741	-1621	Ellipsoid	-15.0	93.6	-70.4	0.0028	Granite
4	724532	776520	-1586	Lens	-2.6	97.7	-86.9	0.001	Qaurtz

magnetic susceptibilities of 0.0754 and 0.0251 respectively suggesting that the bodies causing the anomaly are typical of igneous rocks; basalt and olivine (Telford et al., 1990).

Profile P3 taken in the south eastern part was modeled by Ellipsoid shape emplaced at depth of 1621 m with susceptibility value of 0.0028 (Figure 10), suggesting that the bodies causing the anomaly are typical of intermediate igneous rock; granites (Telford et al., 1990). The Profile P4 taken in the south western part of the study area was modeled with Lens shape emplaced at depth of 1586 m with magnetic susceptibility value of

0.001 (Figure 11), revealing rocks mineral (quartz) (Telford et al., 1990). The blue colour in the modeling map (Figure 7) cannot be modeled. The reason could be as a result of very low total magnetic intensity in the area. Table 1 shows the summary of the modelling result.

Conclusion

The magnetic anomalies of Gashaka and Mayo Daga areas were studied by employing qualitative and quantitative interpretation of aeromagnetic data of the

area. SPI and forward and inverse modeling methods were used as part of quantitative interpretation. From the interpretation method used, the maximum depths obtained from each method were similar and are approximately 2.3 km each. These three depths obtained from SPI, Euler as well as forward and inverse modeling, are good for hydrocarbon accumulation in the study area, and agrees with the assertion of Wright et al. (1985) that the minimum thickness of the sediment required for the commencement of oil formation from marine organic remains would be 2300 m (2.3 km), if other factors are satisfactory.

Through the results from the qualitative and quantitative interpretation obtained from this study, this work has shown some similarities in agreement with those of other researchers (Chinwuko et al., 2013; Wright et al., 1985).

However, this present work could be more reliable in terms of terrain clearance, line spacing and improvement in technology. The aeromagnetic study of the area has helped to delineate the geological structures of Gashaka and Mayo Daga areas which are of great benefits to the solid mineral sector of Nigeria economy.

CONFLICT OF INTERESTS

The authors have not declared any conflict of interests.

REFERENCES

Abbas AA, Mallam A (2013). Estimating the Thickness of Sedimentation within Lower Benue Basin and Upper Anambra Basin, Nigeria, Using Both Spectral Depth Determination and Source Parameter Imaging. Hindawi Publishing Corporation P 10.

Ahmed YM, Oruonye ED (2016). Socioeconomic Impact of Artisanal and Small scale mining on the Mambilla Plateau of Taraba State, Nigeria. World J. Soc. Sci. Res. 3(1).

Briggs IC (1974). Machine contouring using minimum curvature. Geophysics 39:39-48.

Chinwuko AI, Onwuemesi AG, Anakwuba EK, Okeke HC, Onuba LN, Okonkwo CC, Ikumbur EB (2013). Spectral Analysis and Magnetic Modeling over Biu – Damboa, Northeastern Nigeria. IOSR J. Appl. Geol. Geophys. 1(1):20-28.

Dupreez JW, Barber W (1965). The distribution and chemical quality of ground water in Northern Nigeria. Bulletin 36. Geological survey of Nigeria 93.

Frantz C (1981). Development without communities: Social fields, Network and Action in the Mambilla Grasslands of Nigeria. J. Human org. pp. 211-220.

Hamza H, Graba I (2010). Challenges of exploration and utilization of hydrocarbons in the Sokoto Basin. Paper presented at International Conference on the Potentials of Prospecting for Hydrocarbons in the Sokoto Basin on 11th May, 2009 at Usmanu Danfodio University Sokoto, Nigeria.

Jeje LK (1983). Aspects of geomorphology of Nigeria. Heinemann educational books.

Kearey P, Brooks M, Hill I (2002). An Introduction to Geophysical Exploration. (3rd edition). Blackwell Publishing. United Kingdom.

Mould AWS (1960). Report on a rapid reconnaissance soil survey of the Mambilla plateau. Bulletin 15, Soil survey section, regional research station, ministry of agriculture, Samaru, Zaria.

Mubi AM, Tukur AL (2005). Geology and relief of Nigeria. Nigeria. Heinemann educational books.

Naudy H (1970). Method for analyzing aeromagnetic profiles. Geophys. Prospect. 18(1):56-63.

Obiora DN, Yakubu JA, Okeke FN, Chukudebelu JU, Oha AI (2016). Interpretation of Aeromagnetic Data of Idah Area in North Central Nigeria Using Combined Methods. J. Geol. Soc. India 88:98-106.

Ojoh KA (1992). The southern part of the Benue trough (Nigeria) Cretaceous stratigraphy, basin analysis, paleo-oceanography and geodynamic evolution in the equatorial domain of the south Atlantic. NAPE Bull. 7:131-152.

Telford WM, Geldart LP, Sheriff RE (1990). Applied geophysics (2nd edition), Cambridge University press, Cambridge.

Thurston JB, Smith RS (1997). Automatic conversion of magnetic data to depth, dip, and susceptibility contrast using the SPITM method. Geophysics 62(3):807-813.

Tukur AL, Adebayo AA, Galtima A (2005). The land and people of the Mambilla Plateau, Nigeria. Heinemann educational books.

Ugwu GZ, Ezema PO, Eze CC (2013). Interpretation of aeromagnetic data over Okigwe and Afikpo areas of Lower Benue Trough, Nigeria. Int. Res. J. Geol. Mining 3(1):1-8.

Wright JB, Hastings D, Jones WB, Williams HR (1985). Geology and Mineral resources of West Africa. George Allen and Urwin, London.

International Journal of Physical Sciences

Full Length Research Paper

Improvement of the homotopy perturbation method to nonlinear problems

J. F. Alzaidi[1*] and A. A. Alderremy[2]

[1]Department of Mathematics, Faculty of Science, King Abdulaziz University, Jeddah, Saudi Arabia.
[2]Department of Mathematics, Faculty of Science, King Khalid University, Abha, Saudi Arabia.

This paper proposes an effective improvement of the homotopy perturbation method (HPM) by using Jacobi and He's polynomials to solve some nonlinear ordinary differential equations. With this method, the source terms of ordinary differential equations can be expanded in series of shifted Jacobi polynomials. Numerical results are given in this paper to illustrate the reliability of this method with nonlinear ordinary differential equations.

Key words: Homotopy perturbation method (HPM), shifted Jacobi polynomials, nonlinear ordinary differential equations.

INTRODUCTION

In recent years, the subject of differential calculus received attention in regards to effective numerical methods for solving linear and nonlinear differential equations. Examples of these methods are the Adomian decomposition method (ADM) (Wazwaz et al., 2015; Hosseinzadeh et al., 2017), the variational iteration method (Akter and Chowdhury, 2017; Wazwaz, 2015; Glowinski, 2015; Ghorbani and Bakherad, 2017), the pseudospectral method (Bhrawy et al., 2015; Wei et al., 2017; Borluk and Muslu, 2015) and the reproducing kernel Hilbert space method (Arqub et al., 2016).

In 1999, He (1999) proposed the HPM which combines the standard homotopy in topology and perturbation techniques. The HPM is a powerful and effective tool for solving a wide range of problems that arise in various fields. With this method, numerical solutions are

expressed as sums of infinite series. The sums converge rapidly to find solutions.

The HPM can be applied to integro-differential equation (Elbeleze et al., 2016), linear and nonlinear Newell-Whitehead-Segel equations (Nourazar et al., 2017), nonlinear optimal control problems (Jafari et al., 2016), integral equations (Elzaki and Alamri, 2016; Hasan and Matin, 2017), nonlinear wave-like equations with variable coefficients (Gupta et al., 2013), boundary value problems (Opanuga et al., 2017), the quadratic Riccati differential equation (Aminikhah and Hemmatnezhad, 2010), Boussinesq-like equations (Fernández, 2014) and others (Sakar et al., 2016; Soori et al., 2015; Qureshi et al., 2017; Zhang et al., 2014; Najafi and Edalatpanah, 2014; Roy et al., 2015; Abou-Zeid, 2016).

In an overview of approximations of nonlinear ordinary

*Corresponding author. E-mail: j-f-h-z@hotmail.com; aadramy@kku.edu.sa.

differential equations, adomian decomposition method with orthogonal polynomials was proposed as a method for solving nonlinear problems (Liu, 2009). Chun (2010) proposed an efficient modification of the HPM that used Chebyshev's and He's polynomials to solve nonlinear differential equations. Behrooz and Ebadi (2011) further developed the HPM using Legendre polynomials. Recently, Novin and Dastjerd (2015) improved the adomian decomposition method to obtain solutions for the Duffing equation.

This article applies the HPM to the shifted Jacobi polynomials of the right-side function $f(x)$ to solve nonlinear differential equations. The advantage of this approach is that such polynomials are simple and do not require small parameters. Moreover, with a few iterations one can find accurate solutions. To the best of the authors' knowledge, this approach was not employed to solve linear and nonlinear differential equations in the past.

This manuscript is arranged as follows: First, various properties of shifted Jacobi polynomials are presented, followed by a discussion of He's HPM. Thereafter, the proposed HPM is presented along with solutions to three numerical examples and with comparisons of the solutions and results found with other methods; therein, the validity and accuracy of the proposed method is considered. Additionally, the results of the numerical simulation using Maple 17 are given, and the study is concluded.

PROPERTIES OF SHIFTED JACOBI POLYNOMIALS

The well-known standard Jacobi polynomials, $P_k^{(\alpha,\beta)}(x)$ $(\alpha > -1, \beta > -1)$ are defined on the interval $[-1,1]$. The standard Jacobi polynomials of degree k $(P_k^{(\alpha,\beta)}(x), k = 0,1\ldots)$ satisfy the following Rodrigue's formula:

$$P_k^{(\alpha,\beta)}(x) = \frac{(-1)^k}{2^k k!}(1-x)^{-\alpha}(1+x)^{-\beta}\frac{d^k}{dx^k}\left[(1-x)^{\alpha+k}(1+x)^{\beta+k}\right]. (1)$$

For $\alpha = \beta$, one recovers the ultraspherical polynomials (symmetric Jacobi polynomials) and for $\alpha = \beta = \pm\frac{1}{2}, \alpha = \beta = 0$ is the Chebyshev polynomial of the first and second kinds and Legendre polynomials respectively; and for the non-symmetric Jacobi polynomials, the two important special cases $\alpha = -\beta = \pm\frac{1}{2}$ (Chebyshev polynomials of the third and fourth kinds) are also recovered.

The Jacobi polynomials (Bhrawy et al., 2016) satisfy the orthogonality relation.

$$\left(P_k^{(\alpha,\beta)}(x), P_\ell^{(\alpha,\beta)}(x)\right)_{\omega^{(\alpha,\beta)}(x)} = \int_{-1}^{1} P_k^{(\alpha,\beta)}(x) P_\ell^{(\alpha,\beta)}(x)\omega^{(\alpha,\beta)}(x)dx = h_k\delta_{\ell k}, (2)$$

where $\omega^{(\alpha,\beta)}(x) = (1-x)^\alpha(1+x)^\beta$, $h_k = \frac{2^{\alpha+\beta+1}\Gamma(k+\alpha+1)\Gamma(k+\beta+1)}{(2k+\alpha+\beta+1)k!\Gamma(k+\alpha+\beta+1)}$.

In order to use these polynomials on the interval $[0,L]$, we define the so-called shifted Jacobi polynomials by introducing the change of variable $x = \frac{2x}{L} - 1$ Let the shifted Jacobi polynomials $P_i^{(\alpha,\beta)}\left(\frac{2x}{L} - 1\right)$ be denoted by $P_{L,i}^{(\alpha,\beta)}(x)$. Then $P_{L,i}^{(\alpha,\beta)}(x)$ can be obtained with the aid of the following recurrence formula:

$$P_{L,i+1}^{(\alpha,\beta)}(x) = (a_i^{(\alpha,\beta)}(\frac{2x}{L}-1) - b_i^{(\alpha,\beta)})P_{L,i}^{(\alpha,\beta)}(x) - c_i^{(\alpha,\beta)}P_{L,i-1}^{(\alpha,\beta)}(x), \quad i \geq 1, (3)$$

$$P_{L,0}^{(\alpha,\beta)}(x) = 1, \quad P_{L,1}^{(\alpha,\beta)}(x) = \frac{1}{L}(\alpha+\beta+2) x - (\beta+1),$$

where

$$a_i^{(\alpha,\beta)} = \frac{(2i+\alpha+\beta+1)(2i+\alpha+\beta+2)}{2(i+1)(i+\alpha+\beta+1)}$$

$$b_i^{(\alpha,\beta)} = \frac{(\beta^2-\alpha^2)(2i+\alpha+\beta+1)}{2(i+1)(i+\alpha+\beta+1)(2i+\alpha+\beta)}$$

$$c_i^{(\alpha,\beta)} = \frac{(i+\alpha)(i+\beta)(2i+\alpha+\beta+1)}{(i+1)(i+\alpha+\beta+1)(2i+\alpha+\beta)}.$$

The analytic form of the shifted Jacobi polynomials $P_{L,i}^{(\alpha,\beta)}(x)$ of degree i is given by

$$P_{L,i}(x) = \sum_{k=0}^{i}(-1)^{i+k}\frac{\Gamma(i+\beta+1)\Gamma(i+k+\alpha+\beta+1)}{\Gamma(k+\beta+1)\Gamma(i+\alpha+\beta+1)(i-k)!k!L^k}x^k, (4)$$

and the orthogonality condition is

$$\int_0^L P_{L,j}^{(\alpha,\beta)}(x) P_{L,k}^{(\alpha,\beta)}(x)\omega^{(\alpha,\beta)}(x)dx = \hbar_{L,k}^{(\alpha,\beta)}\delta_{jk}, (5)$$

where $\omega_L^{(\alpha,\beta)}(x) = x^\beta(L-x)^\alpha$ and $\hbar_{L,k}^{(\alpha,\beta)} = \frac{L^{\alpha+\beta+1}\Gamma(k+\alpha+1)\Gamma(k+\beta+1)}{(2k+\alpha+\beta+1)k!\Gamma(k+\alpha+\beta+1)}.$

A function $f(x)$, square integrable in $[0,L]$, may be expressed in terms of shifted Jacobi polynomials as

$$f(x) = \sum_{j=0}^{\infty}c_j P_{L,j}^{(\alpha,\beta)}(x),$$

where the coefficients c_j are given by

$$c_j = \frac{1}{\hbar_{L,k}^{(\alpha,\beta)}}\int_0^L f(x) P_{L,j}^{(\alpha,\beta)}(x)\omega_L^{(\alpha,\beta)}(x)dx, \qquad j = 0,1,2,\ldots (6)$$

HE'S HPM

Here, we will present HPM used by He (1999, 2006) to solve nonlinear differential equations that take the following form

$$L(u) + R(u) + N(u) = f(x), \qquad x \in \Omega, \qquad (7)$$

with boundary conditions

$$B\left(u \frac{\partial u}{\partial x}\right) = 0, \qquad x \in \Gamma, \qquad (8)$$

where L is a linear operator of highest order, R is a linear operator of lower order than L, N is a nonlinear operator, B is a boundary operator, $f(x)$ is the source term and Γ is the boundary of the domain Ω. He (1999) defines the homotopy technique as $v(r, p): \Omega \times [0,1] \rightarrow \mathbb{R}$, which satisfies

$$H(v, p) = (1 - p)[L(v) - L(u_0)] + p[L(v) + R(v) + N(v) - f(x)] = 0, \qquad (9)$$

or

$$H(v, p) = L(v) - L(u_0) + p[L(u_0) + L(v) + R(v) + N(v) - f(x)] = 0, \qquad (10)$$

where $p \in [0, 1]$ is an embedding parameter and u_0 is an initial estimated approximation of Equation 7 which satisfies the boundary conditions. Obviously, we have

$$\begin{aligned} H(v, 0) &= L(v) - L(u_0) = 0, \\ H(v, 1) &= L(v) + R(v) + N(v) - f(x) = 0. \end{aligned} \qquad (11)$$

The expansion of p from 0 to 1 is the same as that for $H(v, p)$ from $L(v) - L(u_0)$ to $L(v) + R(v) + N(v) - f(x)$. In topology, this is called deformation and $L(v) - L(u0)$, $L(v) + R(v) + N(v) - f(x)$ are called homotopic. Using the parameter p, we expand the solution of Equation 9 in the following form:

$$v = v_0 + pv_1 + p^2v_2 + p^3v_3 + \dots \qquad (12)$$

When $p \rightarrow 1$, Equation 12 becomes the approximate solution of Equation 7, that is,

$$u = \lim_{p \to 1} v = v_0 + v_1 + v_2 + v_3 + \dots \qquad (13)$$

METHODOLOGY OF HPM BASED ON SHIFTED JACOBI POLYNOMIALS

When implementing the previous HPM on some problems we find that the source term $f(x)$ is not easy to integrate. So, in this paper, for an arbitrary natural number N, $f(x)$ can be expressed in the

shifted Jacobi series

$$f(x) \approx f_{(J,N)}(x) = \sum_{i=0}^{N} a_i P_{L,i}^{(\alpha, \beta)}(x) \qquad (14)$$

To deal with the nonlinear term $N(u)$, we will use He's polynomials

$$N(v_0, v_1, \dots, v_n) = \frac{1}{n!} \frac{\partial^n}{\partial p^n} N\left(\sum_{j=0}^{n} p^j v_j\right)_{p=0}, \qquad (15)$$

and satisfy the following relation

$$N(v) = N(v_0) + pN(v_0, v_1) + p^2 N(v_0, v_1, v_2) + \dots + p^n N(v_0, v_1, v_2, \dots, v_n) + \dots \qquad (16)$$

Substituting Equations 12, 14 and 16 into 10, and equating coefficients of like powers of p, we get

$$\begin{aligned} p^0 &: L(v_0) - L(u_0) = 0, \\ p^1 &: L(v_1) + L(u_0) + R(v_0) + N(v_0) - f_{(J,N)}(x) = 0, \\ p^2 &: L(v_2) + R(v_1) + N(v_0, v_1) = 0, \\ p^3 &: L(v_3) + R(v_2) + N(v_0, v_1, v_2) = 0, \\ &\vdots \\ p^{n+1} &: L(v_{n+1}) + R(v_n) + N(v_0, v_1, v_2, \dots, v_n) = 0, \end{aligned} \qquad (17)$$

and so on. By solving the above set equations with suitable initial conditions, $v_0, v_1, v_2, \dots, v_n$ can be determined and the series solution (12) will be entirely determined. The N-term approximation solution of Equation 7 can be considered as follows

$$U_N = \sum_{k=0}^{N-1} v_k. \qquad (18)$$

NUMERICAL SIMULATION AND COMPARISONS

Here, several numerical examples to demonstrate the high accuracy and applicability of the proposed methods for solving nonlinear ordinary differential equations are presented. We also compare the results given from our method and those reported in the literature. The comparisons reveal that our methods are very effective and convenient.

Example 1

We consider the following equation (Liu, 2009; Behrooz and Ebadi, 2011)

$$u'' + xu' + x^2 u^3 = (2 + 6x^2)e^{x^2} + x^2 e^{3x^2}, \qquad 0 \le x \le 1, \quad (19)$$

$$u(0) = 1, \ u'(0) = 0, \qquad (20)$$

with exact solution $u(x) = e^{x^2}$.
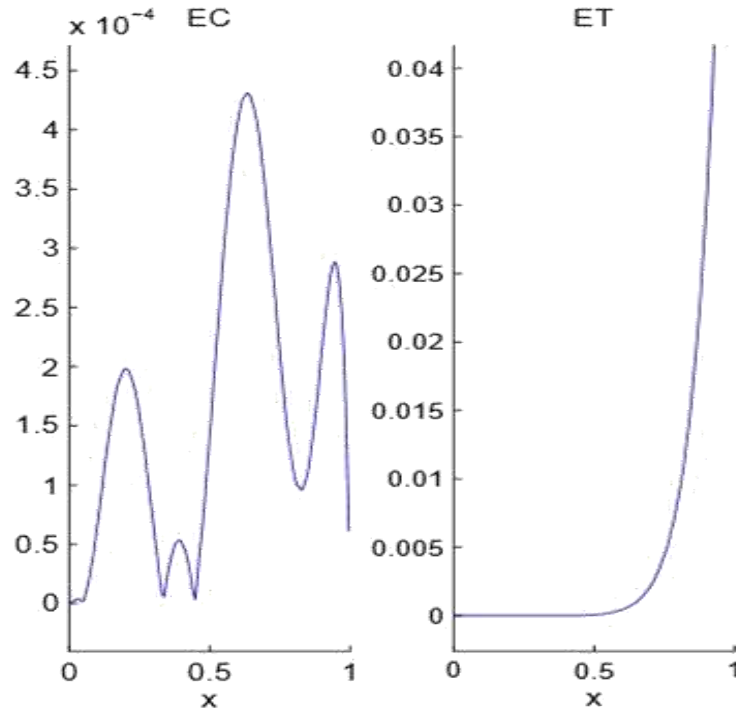
Figure 1. AEs of HPM by Chebyshev (EC) and Taylor (ET) polynomials at $N = 6$ for Example 1.
Source: Behrooz and Ebadi (2011).

In an operator form, Equation 19 can be written as:

$$L(u)+R(u)+N(u)=f(x), \quad (21)$$

where $L = \frac{d}{dx^2}$, $R(u) = x\frac{d}{dx}u$, $N(u) = x^2 u^3$ and $f(x) = (2 + 6x^2)\,e^{x^2} + x^2 e^{3x^2}$.

Behrooz and Ebadi (2011) introduced this problem and presented Figure 1 to show the absolute errors (AEs) of HPM with Chebyshev and Taylor polynomials at $N = 6$. Moreover, Liu (2009) applied the ADM with Legendre, Chebyshev and Taylor polynomials to this problem and presented the absolute errors (AEs) in Figures 2, 3 and 4. Now, we apply our method for this problem.
   The homotopy equation is

$$v'' - L(u_0) + pL(u_0) + p[R(v)+N(v)-f(x)]=0, \quad (22)$$

where

$$v = \sum_{i=0}^{\infty} p^i v_i(x). \quad (23)$$

According to Equation 15, He's polynomials are found to be:

$$N(v_0)=x^2 v_0^3,$$
$$N(v_0,v_1)=x^2(3v_0^2 v_1),$$
$$N(v_0,v_1,v_2)=x^2(3v_0^2 v_2 + 3v_0 v_1^2),$$
$$N(v_0,v_1,v_2,v_3)=x^2(3v_0^2 v_3 + 6v_0 v_1 v_2 + v_1^3),$$
$$N(v_0,v_1,v_2,v_3,v_4)=x^2(3v_1^2 v_2 + 3v_0 v_2^2 + 6v_0 v_1 v_3 + 3v_0^2 v_4),$$
$$N(v_0,v_1,v_2,v_3,v_4,v_5)=x^2(3v_1 v_2^2 + v_1^2 v_3 + 6v_0 v_2 v_3 + 6v_0 v_1 v_4 + 3v_0^2 v_5),$$
$$\vdots$$
$$\quad (24)$$

Substituting relations Equation 24 in Equation 16, gives the following relation

$$N(v) = x^2 v_0^3 + x^2(3v_0^2 v_1)p + x^2(3v_0^2 v_2 + 3v_0 v_1^2)p^2 + x^2(3v_0^2 v_3 + 6v_0 v_1 v_2 + v_1^3)p^3 + \ldots \quad (25)$$

Now, if $\alpha = \beta = \dfrac{1}{20}$ and $N = 6$ the expansions of $f(x)$ in shifted Jacobi polynomials are obtained by

$$f_{(J,6)}(x) \approx 2.075653430 - 3.81896575x + 55.6619634x^2 - 229.6216407x^3 + 544.8167168x^4 - 595.0415693x^5 + 267.6207961x^6. \quad (26)$$

Substituting Equation 25 and Equation 23 into the homotopy (22) and equating the terms with identical powers of p, gives:
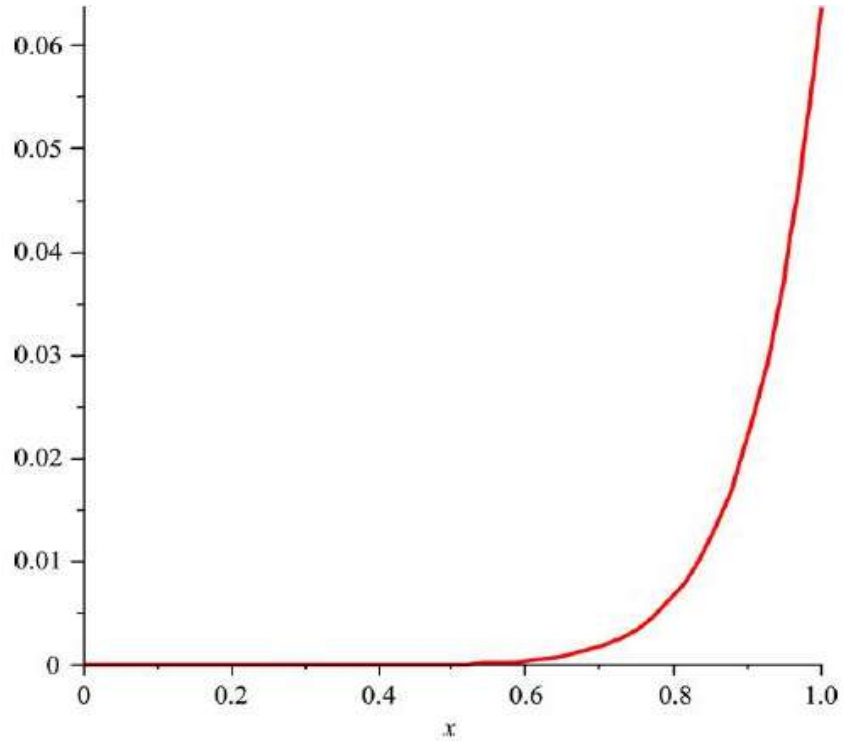
Figure 2. AEs of ADM by Taylor polynomials at $N = 6$ for Example 1.
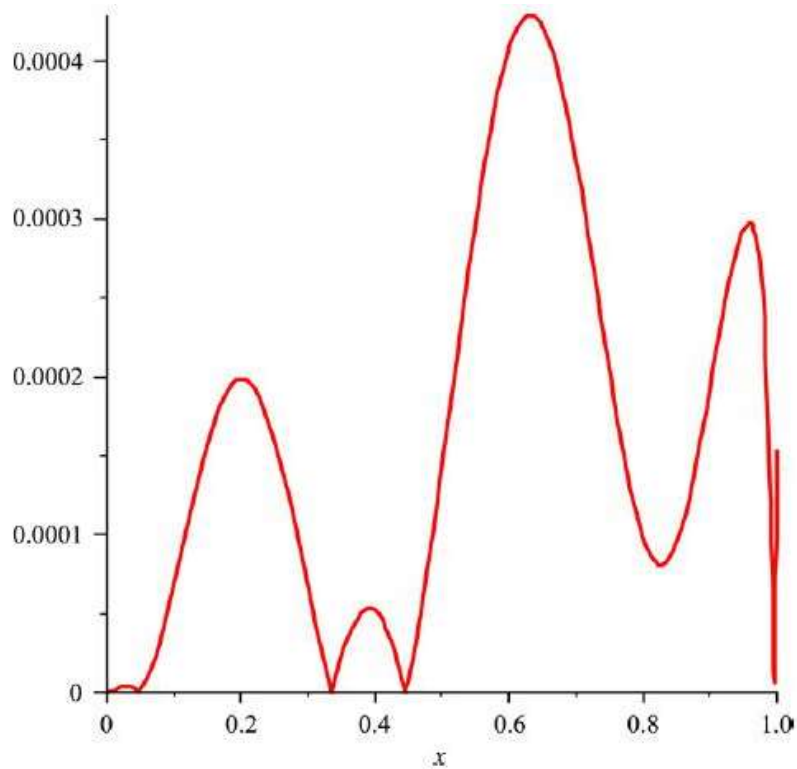Source: Behrooz and Ebadi (2011).

Figure 3. AEs of ADM by Chebyshev polynomials at $N = 6$ for Example 1.
Source: Liu (2009).
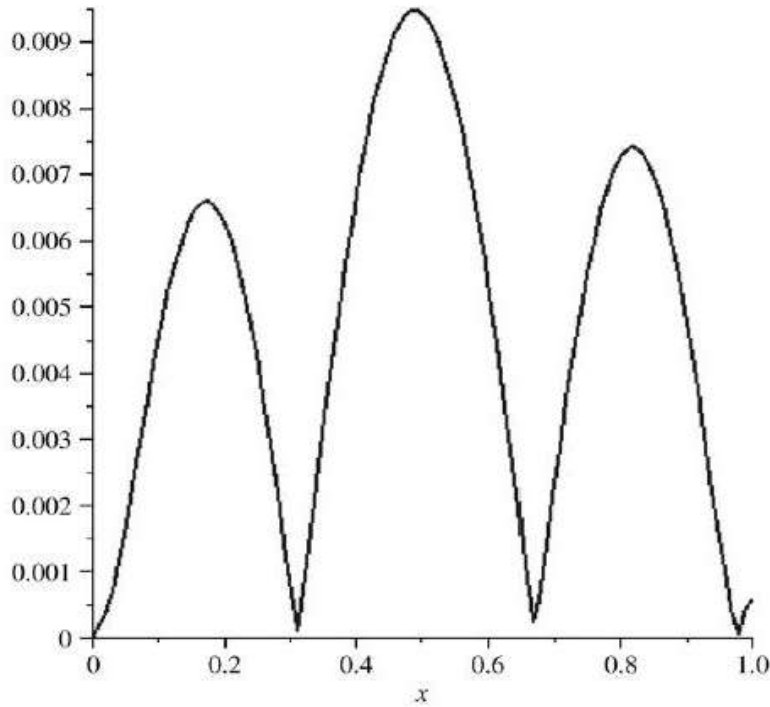
Figure 4. AEs of ADM by Legendre polynomials at $N = 6$ for Example 1.
Source: Liu (2009).

$$p^0 : \begin{cases} v'' - 2 = 0, \\ v_0(0) = 1, \quad v_0'(0) = 0, \end{cases}$$

$$p^1 : \begin{cases} v_1'' + 2 + x v_0' + x^2 v_0^3 - f_{(J,6)}(x) = 0, \\ v_1(0) = 0, \quad v_1'(0) = 0, \end{cases}$$

$$p^2 : \begin{cases} v_2'' + 3x^2 v_0^2 v_1 + x v_1' = 0, \\ v_2(0) = 0, \quad v_2'(0) = 0, \end{cases}$$

$$p^3 : \begin{cases} v_3'' + 3x^2 (v_0^2 v_2 + v_0 v_1^2) + x v_2' = 0, \\ v_3(0) = 0, \quad v_3'(0) = 0, \end{cases}$$

$$p^4 : \begin{cases} v_4'' + x v_3' + x^2 (3v_0^2 v_3 + 6v_0 v_1 v_2 + v_1^3) = 0, \\ v_4(0) = 0, \quad v_4'(0) = 0, \end{cases}$$

$$p^5 : \begin{cases} v_5'' + x v_4' + x^2 (3v_0^2 v_4 + 6v_0 v_1 v_3 + 3v_0 v_2^2 + 3v_1^2 v_2) = 0, \\ v_5(0) = 0, \quad v_5'(0) = 0, \end{cases}$$

$$p^6 : \begin{cases} v_6'' + x v_5' + x^2 (3v_0^2 v_5 + 6v_0 v_1 v_4 + 6v_0 v_2 v_3 + 3v_1^2 v_3 + 3v_1 v_2^2) = 0, \\ v_6(0) = 0, \quad v_6'(0) = 0. \end{cases} \quad (27)$$

By substituting Equation 26 in $f_{(J,6)}(x)$ at Equation 27, and solving the above equations by the help of Maple, we obtain

$$\begin{aligned} u(x) &= 1 + 1.037826715 x^2 - 0.6364942917 x^3 + 4.382192498 x^4 + \dots \\ &\quad + 8.685292246 \times 10^{-7} x^{46} + 5.764802911 \times 10^{-9} x^{47} - 1.642452152 \times 10^{-9} x^{48} \\ &\quad + 1.024528074 \times 10^{-12} x^{50}. \end{aligned} \quad (28)$$

The absolute error of HPM with shifted Jacobi polynomials at $N = 6$ is plotted in Figure 5.

The accuracy of this method is validated by comparing to the exact $u(x)$. By comparing Figures 1 to 5, it is found that the absolute errors (AEs) generated using our method are smaller than the errors caused by HPM with Chebyshev (EC) and Taylor (ET) polynomials and by ADM with Legendre, Chebyshev and Taylor polynomials. This means that the method here is more accurate than previous methods.

Example 2

We consider the following problem (Behrooz and Ebadi, 2011):

$$u'' + u u' = x \sin(2x^2) - 4x^2 \sin(x^2) + 2 \cos(x^2), \quad (29)$$

$$u(0) = 0, \quad u'(0) = 0, \qquad 0 \leq x \leq 1, \quad (30)$$

with exact solution $u(x) = \sin(x^2)$. In an operator form, Equation 29 can be written as:

$$L(u) + N(u) = f(x), \quad (31)$$

where $L = \dfrac{d}{dx^2}$, $N(u) = u u'$ and $f(x) = x \sin(2x^2) - 4x^2 \sin(x^2) + 2 \cos(x^2)$.

The homotopy equation is:
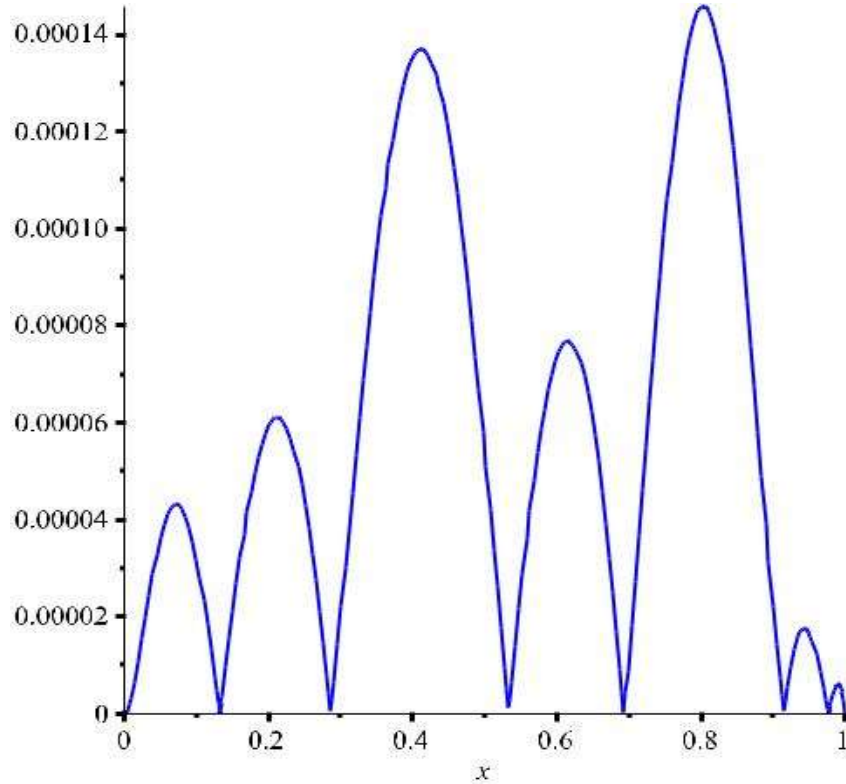
Figure 5. AEs of HPM by shifted Jacobi polynomials at $\alpha = \beta = \frac{1}{20}$ and $N = 6$ for Example 1.

$$v'' - L(u_0) + p L(u_0) + p[N(v) - f(x)] = 0. \qquad (32)$$

He's polynomials for the nonlinear term $N(u) = uu'$ are found to be

$$
\begin{aligned}
N(v_0) &= v_0 v_0', \\
N(v_0, v_1) &= v_0 v_1' + v_1 v_0', \\
N(v_0, v_1, v_2) &= v_0 v_2' + v_1 v_1' + v_2 v_0', \\
N(v_0, v_1, v_2, v_3) &= v_0 v_3' + v_1 v_2' + v_2 v_1' + v_3 v_0', \\
N(v_0, v_1, v_2, v_3, v_4) &= v_0 v_4' + v_1 v_3' + v_2 v_2' + v_3 v_1' + v_4 v_0', \\
&\ \vdots
\end{aligned}
\qquad (33)
$$

Now, if $\alpha = \beta = \frac{1}{20}$ and $N = 20$ the expansions of $f(x)$ in shifted Jacobi polynomials are obtained by

$$
\begin{aligned}
f_{(J,10)}(x) \approx\ & 1.999997823 + 0.26993648 \times 10^{-3} x - 0.8403435 \times 10^{-2} x^2 + 2.112845335 x^3 \\
& - 5.80766750 x^4 + 3.416658954 x^5 - 8.977727745 x^6 + 13.49519614 x^7 \\
& - 14.20329364 x^8 + 8.284749236 x^9 - 1.688604332 x^{10}.
\end{aligned}
\qquad (34)
$$

Substituting Equation 23 and using Equation 16 with relations

33 into the homotopy Equation 32 and equating the terms with identical powers of p, gives

$$
\begin{aligned}
p^0 : &\begin{cases} v_0'' - 2 = 0, \\ v_0(0) = 0, \quad v_0'(0) = 0, \end{cases} \\[4pt]
p^1 : &\begin{cases} v_1'' + 2 + v_0 v_0' - f_{(J,10)}(x) = 0, \\ v_1(0) = 0, \quad v_1'(0) = 0, \end{cases} \\[4pt]
p^2 : &\begin{cases} v_2'' + v_0' v_1 + v_0 v_1' = 0, \\ v_2(0) = 0, \quad v_2'(0) = 0, \end{cases} \\[4pt]
p^3 : &\begin{cases} v_3'' + v_1 v_1' + v_0' v_2 + v_0 v_2' = 0, \\ v_3(0) = 0, \quad v_3'(0) = 0, \end{cases} \\
&\ \vdots
\end{aligned}
\qquad (35)
$$

$$
p^{10} : \begin{cases} v_{10}'' + v_1' v_8 + v_2' v_7 + v_3' v_6 + v_4' v_5 + v_4 v_5' + v_3 v_6' + v_2 v_7' + v_1 v_8' + v_0' v_9 + v_0 v_9', \\ v_{10}(0) = 0, \quad v_{10}'(0) = 0. \end{cases}
$$

By substituting Equation 34 in $f_{(J,10)}(x)$ at Equation 35, and solving the above equations by the help of Maple, we obtain

$$
\begin{aligned}
u(x) =\ & 0.9999989115 x^2 + 0.4498941333 \times 10^{-4} x^3 - 0.7002862500 \times 10^{-3} x^4 \\
& + 0.5642484450 \times 10^{-2} x^5 + \cdots - 2.229469520 \times 10^{-13} x^{64} + 2.357695514 \times 10^{-14} x^{65} \\
& - 1.572944876 \times 10^{-15} x^{66} + 4.949801810 \times 10^{-17} x^{67}.
\end{aligned}
\qquad (36)
$$
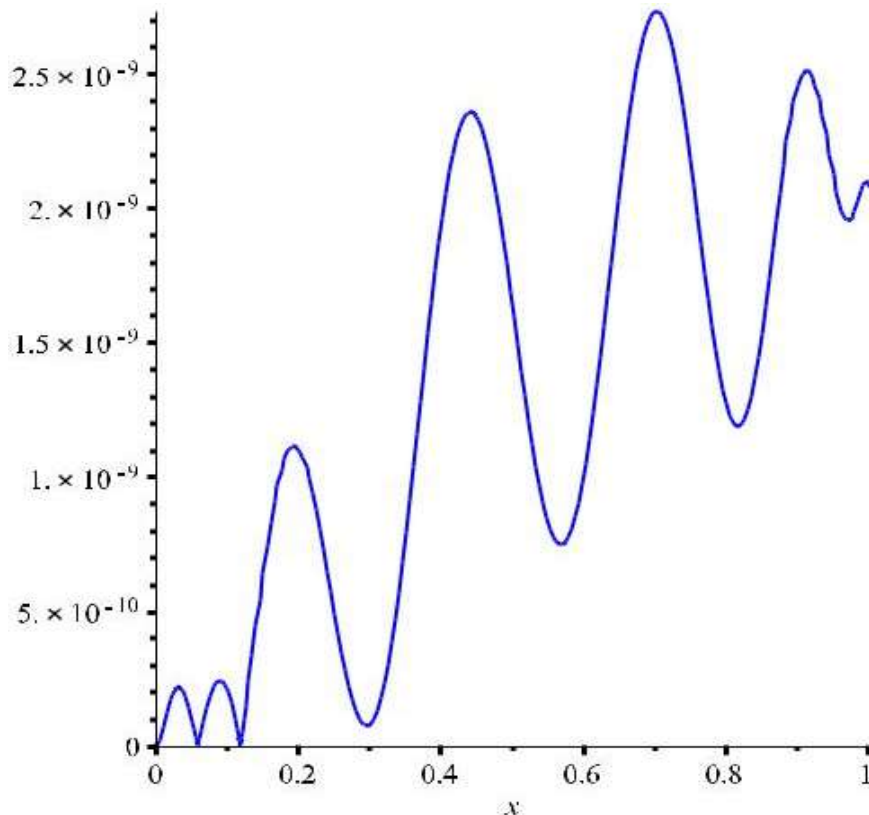
Figure 6. AEs of HPM by shifted Jacobi polynomials at $N = 10$ and $\alpha = \beta = \frac{1}{20}$ for Example 2.

The absolute errors (AEs) at $\alpha = \beta = \dfrac{1}{20}$ and $N = 10$ are presented in Figure 6 which showed that the results of HPM with shifted Jacobi polynomials to be more accurate results than the results of HPM with Legendre, Chebyshev and Taylor polynomials (Behrooz and Ebadi, 2011) represented in Figure 7.

Example 3

Consider the equation (Behrooz and Ebadi, 2011; Novin and Dastjerd, 2015),

$$u'' + 3u - 2u^3 = \cos(x)\sin(2x), \tag{37}$$

$$u(0) = 0, \quad u'(0) = 1, \quad 0 \leq x \leq 1. \tag{38}$$

The exact solution of this problem is $u(x) = sin(x)$. In an operator form, Equation 37 can be written as:

$$L(u) + R(u) + N(u) = f(x), \tag{39}$$

where $L = \dfrac{d}{dx^2}$, $R(u) = 3u$, $N(u) = -2u^3$ and $f(x) = \cos(x)\sin(2x)$.

The homotopy equation is:

$$v'' - L(u_0) + p\,L(u_0) + p[R(v) + N(v) - f(x)] = 0. \tag{40}$$

Similar to the previous two examples, if $\alpha = -0.01, \beta = -0.005$ and $N = 7$, we get

$$\begin{aligned}f_{(J,7)}(x) &\approx 0.5196100000 \times 10^{-5} + 2.000385742x - 0.6852219400 \times 10^{-2}x^2 \\ &\quad - 2.282885057x^3 - 0.1876329186x^4 + 1.396156963x^5 \\ &\quad - 0.4115735108x^6 - 0.01630481208x^7.\end{aligned} \tag{41}$$

The approximate solutions

$$\begin{aligned}u(x) &= x - 0.2598050000 \times 10^{-5}x^2 - 0.1666023763x^3 - 0.5703687707 - 10^{-3}x^4 \\ &\quad + \cdots - 4.353096806 \times 10^{-20}x^{47} - 6.612018552 \times 10^{-22}x^{48} - 3.742005363 \times 10^{-24}x^{49}.\end{aligned} \tag{42}$$

In Table 1, we compare the AEs achieved using our method with those obtained using the ADM with Legendre and Taylor polynomials (Novin and Dastjerd, 2015) at $N = 7$. Figure 8 plot the AEs of the HPM with shifted Jacobi polynomials, which show that our method

Figure 7. AEs of HPM by Legendre (EL), Chebyshev (EC) and Taylor (ET) polynomials for Example 2.
Source: Behrooz and Ebadi (2011).

Table 1. Comparison of our method with the ADM with Legendre and Taylor polynomials (Novin and Dastjerd, 2015) at $\alpha = -0.01$, $\beta = -0.005$ and $N = 7$ for Example 3.

x	Our method	ADM with Legendre polynomials	ADM with Taylor polynomials
0.2	1.9×10^{-9}	2.012×10^{-9}	5×10^{-12}
0.4	1×10^{-10}	1.16×10^{-10}	1.0224×10^{-8}
0.6	6×10^{-10}	1.951×10^{-9}	8.70197×10^{-7}
0.8	2.7×10^{-9}	4.3981×10^{-7}	1.9931859×10^{-5}
1	2.50×10^{-8}	1.36581×10^{-6}	$2.32196948 \times 10^{-4}$

is more accurate than HPM with Chebyshev and Taylor polynomials (Behrooz and Ebadi, 2011) shown in Figure 9.

From Table 1, Figures 8 and 9 listed above, it is shown that the method here is surpassed than ADM with Legendre and Taylor polynomials introduced by Novin and Dastjerd (2015) and the HPM with Chebyshev and Taylor polynomials introduced by Behrooz and Ebadi (2011).

perturbation algorithm has been proposed to find an accurate numerical solution for the nonlinear ordinary differential equations. The core of the proposed method was the source term that can be expressed in the shifted Jacobi series. By comparing the approximate solutions of the problems in this research with their exact solutions and with the approximate solutions achieved by other methods, the validity and accuracy of the scheme of this research is confirmed.

Conclusions

In this work, a generalization to the homotopy

CONFLICT OF INTERESTS

The authors have not declared any conflict of interests.

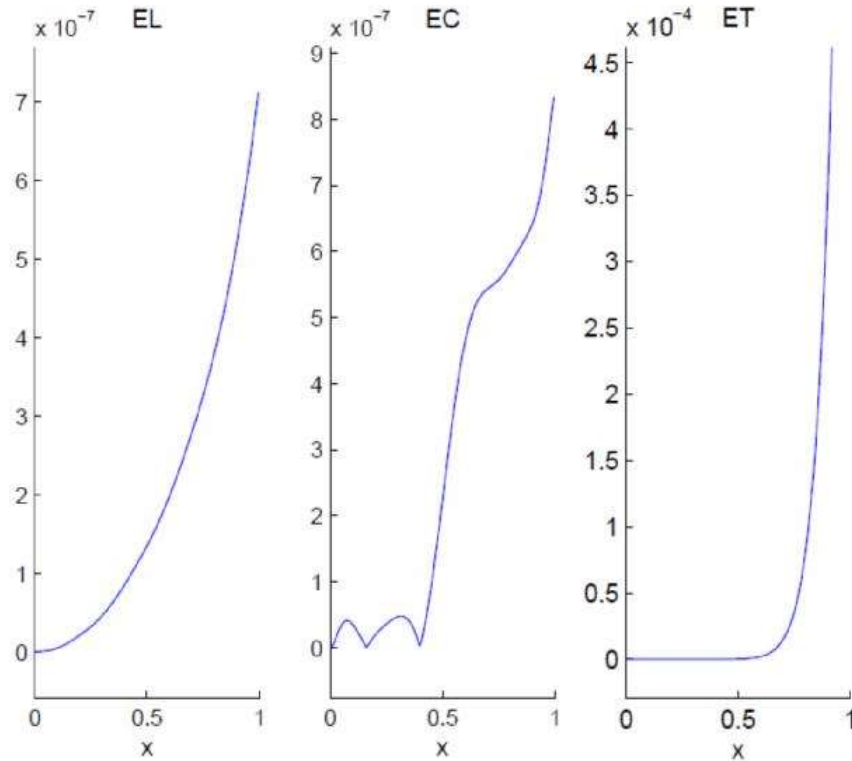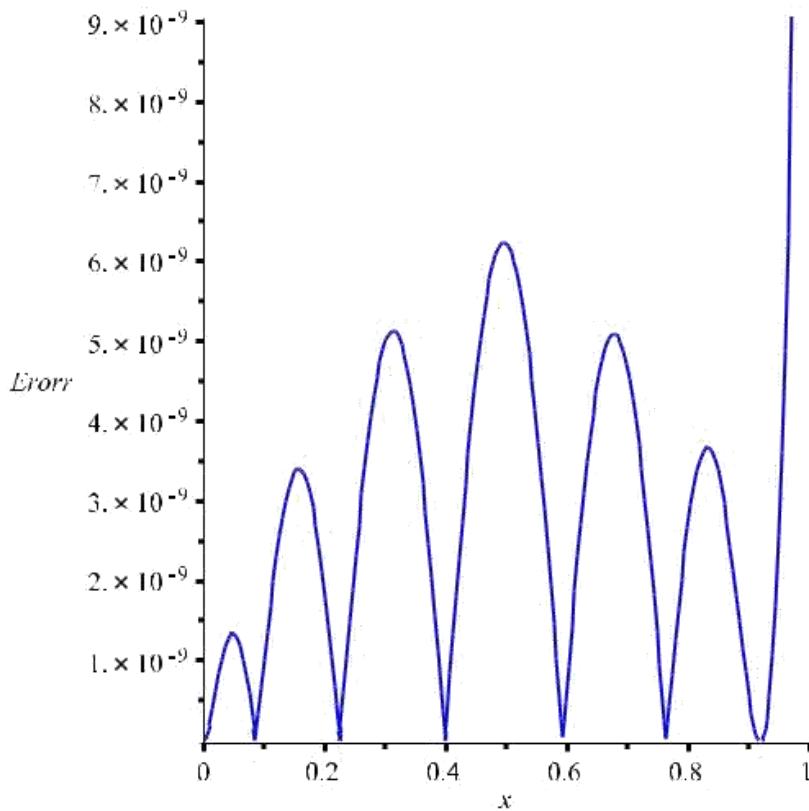**Figure 8.** AEs of HPM by shifted Jacobi polynomials at $\alpha = -0.01, \beta = -0.005$ and $N = 7$ for Example 3.
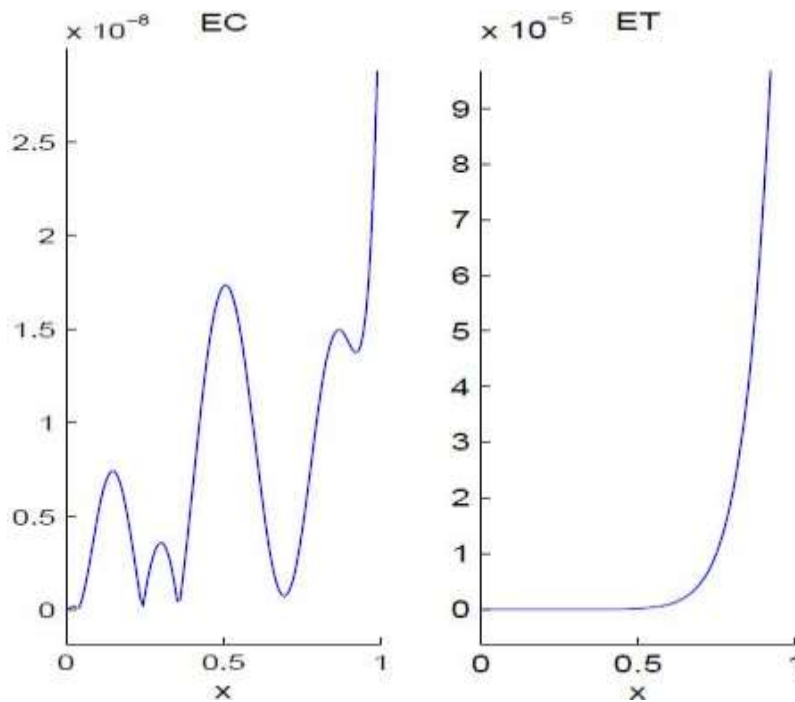

Figure 9. AEs of HPM by Chebyshev (EC) and Taylor (ET) polynomials for Example 3.
Source: Behrooz and Ebadi (2011).

ACKNOWLEDGEMENTS

REFERENCES

Abou-Zeid M (2016). Effects of thermal-diffusion and viscous dissipation on peristaltic flow of micropolar non-Newtonian nanofluid: Application of homotopy perturbation method. Results Phys. 6:481-495.

Akter MT, Chowdhury MM (2017). Variational iteration method for solving coupled Schrödinger-Klein-Gordon equation. Am. J. Comput. Appl. Math. 7(1):25-31.

Aminikhah H, Hemmatnezhad M (2010). An efficient method for quadratic Riccati differential equation. Commun. Nonlinear Sci. Numer. Simul.15(4):835-839.

Arqub OA, Mohammed AS, Momani S, Hayat T (2016). Numerical solutions of fuzzy differential equations using reproducing kernel Hilbert space method. Soft Comput. 20(8):3283-3302.

Behrooz SF, Ebadi G (2011). Homotopy perturbation method based on orthogonal polynomials. Int. J. Nonlinear Sci. 12(2):205-213.

Bhrawy AH, Alzaidy JF, Abdelkawy MA, Biswas A (2016). Jacobi spectral collocation approximation for multi-dimensional time-fractional Schrödinger equations. Nonlinear Dyn. 84(3):1553-1567.

Bhrawy AH, Hafez RM, Alzaidy JF (2015). A new exponential Jacobi pseudospectral method for solving high-order ordinary differential equations. Adv. Differ. Equ. 2015(1):1-15.

Borluk H, Muslu GM (2015). A fourier pseudo-spectral method for a generalized improved boussinesq equation. Numer. Methods Partial Differ. Equ. 31(4):995-1008.

Chun C (2010). Application of homotopy perturbation method with Chebyshev polynomials to nonlinear problems. Zeitschrift für Naturforschung A. 65(1-2):65-70.

Elbeleze AA, Kilicman A, Taib BM (2016). Approximate solution of integro differential equation of fractional (arbitrary) order. J. King Saud Univ. Sci. 28(1):61-68.

Elzaki TM, Alamri AS (2016). Note on new homotopy perturbation method for solving non-linear integral equations. J. Math. Comput. Sci. 6(1):149-155.

Fernández FM (2014). On the homotopy perturbation method for boussinesq-like equations. Appl. Math. Comput. 230:208-210.

Ghorbani A, Bakherad M (2017). A variational iteration method for solving nonlinear lane-emden problems. New Astron. 54:1-6.

Glowinski R (2015). Variational methods for the numerical solution of nonlinear elliptic problems. SIAM.

Gupta S, Kumar D, Singh J (2013). Application of He's homotopy perturbation method for solving nonlinear wave-like equations with variable coefficients. Int. J. Adv. Appl. Math. Mech. 1(2):65-79.

Hasan MM, Matin MA (2017). Approximate solution of nonlinear integral equations of the second kind by using homotopy perturbation method. Dhaka Univ. J. Sci. 65(2):151-155.

He JH (1999). Homotopy perturbation technique. Comput. Methods Appl. Mech. Eng. 178(3):257-262.

He JH (2006). Addendum: new interpretation of homotopy perturbation method. Int. J. Modern Phys. B. 20(18):2561-2568.

Hosseinzadeh H, Jafari H, Gholami MR, Ganji DD (2017). Solving a class of boundary value problems in structural engineering and fluid mechanics using homotopy perturbation and adomian decomposition methods. Italian J. Pure Appl. Math. 37:687-698.

Jafari H, Ghasempour S, Baleanu D (2016). On comparison between iterative methods for solving nonlinear optimal control problems. J. Vib. Control. 22(9):2281-2287.

Liu Y (2009). Adomian decomposition method with orthogonal polynomials: Legendre polynomials. Math. Comput. Model. 49(5):1268-1273.

Najafi HS, Edalatpanah S (2014). Homotopy perturbation method for linear programming problems. Appl. Math. Model. 38(5):1607-1611.

Nourazar S, Parsa H, Sanjari A (2017). A comparison between Fourier transform Adomian decomposition method and homotopy perturbation method for linear and non-linear Newell-Whitehead-Segel equations. AUT J. Model. Simul. 64:111-120.

Novin R, Dastjerd ZS (2015). Solving Dung equation using an improved semi-analytical method. Commun. Adv. Comput. Sci. Appl. 2015(2):54-58.

Opanuga AA, Owoloko EA, Agboola OO, Okagbue HI (2017). Application of homotopy perturbation and modified Adomian decomposition methods for higher order boundary value problems. Lecture Notes in Engineering and Computer Science: Proceedings of The WCE. London. U.K. 1:130- 134.

Qureshi MI, Hashmi M, Iqbal S (2017). A study of obstacle problems using homotopy perturbation method. J. National Sci. Found. Sri Lanka. 45(4):337-346.

Roy PK, Das A, Mondal H, Mallick A (2015). Application of homotopy perturbation method for a conductive-radiative fin with temperature dependent thermal conductivity and surface emissivity. Ain Shams Eng. J. 6(3):1001-1008.

Sakar MG, Uludag F, Erdogan F (2016). Numerical solution of time-fractional nonlinear PDEs with proportional delays by homotopy perturbation method. Appl. Math. Model. 40(13):6639-6649.

Soori M, Nourazar SS, Nazari-Golshan A (2015). Application of the variational iteration method and the homotopy perturbation method to the Fisher type equation. Int. J. Math. Comput. 27(3):1-9.

Wazwaz AM (2015). Solving two emden-fowler type equations of third order by the variational iteration method. Appl. Math. Inf. Sci. 9(5):2429-2436.

Wazwaz AM, Rach R, Duan JS (2015). Solving New Fourth–Order Emden–Fowler- Type Equations by the Adomian Decomposition Method. Int. J. Comput. Methods Eng. Sci. Mech.16(2):121-131.

Wei S, Zou Y, Sun F, Christopher O (2017). A pseudospectral method for solving optimal control problem of a hybrid tracked vehicle. Appl. Ener.194:588-595.

Zhang X, Zhao J, Liu J, Tang B (2014). Homotopy perturbation method for two dimensional time-fractional wave equation. Appl. Math. Model. 38(23):5545-5552.

Full Length Research Paper

Investigation of gravity anomalies in parts of Niger Delta Region in Nigeria using aerogravity data

Ekpa M. M. M.[1], Okeke F. N.[2], Ibuot J. C.[2*], Obiora D. N.[2] and Abangwu U. J.[2]

[1]Department of Physics, School of Science Education, Federal College of Education (Technical), Omoku, Rivers State, Nigeria.
[2]Department of Physics and Astronomy, Faculty of Physical Sciences, University of Nigeria, Nsukka, Enugu State, Nigeria.

Gravity anomalies in parts of the Niger Delta region, Nigeria, were investigated through the interpretation of aerogarvity data with the objectives to determine the thickness of the sedimentary basin, establish the basement topography, density contrasts and the geological models which will give information about variation of geological structures. Four sheets of digital airborne gravity data were used for the study. Source parameter imaging (SPI), Standard Euler deconvolution and forward and inverse modeling techniques were employed in quantitative interpretation. The Bouguer anomaly of the study area varied from -20.0 to 37.7 mGal, while the residual Bouguer anomaly varied from -19.6 to 25.7 mGal. The SPI gave depth values ranging from -539.7 to -4276.0 m for shallow and deep lying gravity anomalous bodies. The windowed Euler-3D for Bouguer gravity result revealed the depth range of 1355.5 to -1518.1 m for structural index of one; 2384.5 to -3283.2 m for structural index of two and 2426.0 to -5011 m for structural index of three. The forward and inverse modeling gave the density values for the modeled profiles 1, 2, 3, 4 and 5 as 1.820, 2.410, 0.720, 2.310 and 2.100 gcm^{-3}, respectively, with their respective depths of 3872, 4228, 4880, 3560 and 2527 m. The results from this study have shown that the depth to basement and density contrast have influence on the petroleum/hydrocarbon accumulation.

Key words: Aerogravity, basement, density contrast, sedimentary.

INTRODUCTION

The gravity survey is a non-destructive geophysical technique that measures difference in the earth's gravitational field at specific locations. It could be ground gravity survey or airborne (aero) gravity survey. In geosciences, the gravity method has been widely used in different applications involving engineering exploration, regional and large scales study of geological structures, where measurements of earth's gravitational field are used to map subsurface variations in density (Biswas and Sharma, 2016; Biswas et al., 2014a, b; Mandal et al., 2015, 2013). The anomalies in the earth's gravitational field results from lateral variations in the density of subsurface rocks and the distance from the measuring point. Factors like grain density, porosity and interstitial

*Corresponding author. E-mail: johnson.ibuot@unn.edu.ng.

fluids within materials affect density contrast. Gravity data can be used in many ways to solve different exploration problems, depending on the geologic setting and rock parameters (Ezekiel et al., 2013; Okiwelu et al., 2013; Obiora et al., 2016), the data when analyzed provide insight to elements of petroleum exploration and production (Johnson, 1998; Obiora et al., 2016). The density contrasts presented by the juxtaposition of sediments with shales make detailed gravity modeling in this region a valuable exercise. The aerogravity method has found numerous applications in engineering and environmental studies including locating voids and karst features, buried stream valleys, water table and determination of soil layer thickness. The success of the gravity method depends on the different earth materials having different bulk densities (mass) that produced variations in the measured gravitational field. The gravity method has good depth penetration compared to ground penetration radar, high frequency electromagnetic and dc-resistivity techniques and is not affected by high conductivity values of near-surface clay rich soils (Mickus, 2004).

The aerogravity data are acquired with sufficient resolution which contributes towards resource-scale projects which can be used to characterize salt domes for petroleum exploration, geothermal energy investigations, monitoring of geothermal reservoirs under exploitation, inferring location of faults, and permeable areas for hydrothermal movement (Adedapo et al., 2014; Agunleti and Salua, 2015). There is generally an ambiguity in all geophysics data interpretation, this affects all geophysical data and the ambiguities that arise from different geologic configurations producing similar observed measurements (Biswas, 2015, 2016, 2017a, b; Mbah et al., 2017; Biswas et al., 2017; Singh and Biswas, 2016; Biswas and Sharma, 2015, 2014a, b; Sharma and Biswas, 2013). According to Hospers (1965), the gravity field of Niger Delta showed negative values of low magnitude covering most parts of the Niger Delta and these low values are referred to as Niger Delta minimum. Depth to basement investigation is necessary in exploration as it gives information about where matured hydrocarbons are found. The objectives of this study were to determine the thickness of the sedimentary basin, establishing the basement topography and the geological models to give information about the variation of the geological structures.

Location and geology of the Niger Delta

The study area is located in the Niger Delta region which is found in the Gulf of Guinea (Tuttle et al., 1999); it is one of the most prolific hydrocarbon basins in the world. The towns covered in the study were Olobirin, Degema, Patani and Ahoada. Niger Delta has an area of about 300,000 km^2, sediment thickness of over 10,000 km and

sediment volume of 500,000 km^3 (Okiwelu et al., 2013). Niger Delta is located between latitudes 3°30' and 4°30'N, longitude 6°00' and 7°00'E. Niger Delta sediments are divided into three distinct units of Eocene to Recent ages that form major transgressive and regressive cycles. Marine sedimentation started to evolve in the early Tertiary times according to Doust and Omatsola (1990) and over the years it has prograded a distance of more than 250 km from the Benin and Calabar flanks to the present delta front, controlled by synsedimentary faults, folding and subsidence with sediment supply mainly from the Niger, Benue and Cross Rivers accumulating up to 12,000 m thickness in some regions (Merki, 1972; Evamy et al., 1978).

The Niger Delta generally displays three vertical lithostratigraphic subdivisions: an upper delta top facies; a middle delta front lithofacies; and a lower pro-delta lithofacies. These lithostratigraphic units correspond, respectively with the continental sands of Benin Formation (Oligocencene-Recent), the alternating sand/shale paralic of Agbada formation (Eocene-Recent) and the marine prodeltashales of Akata formation (Paleocene-Recent). The sands and sandstones of Agbada formation are the main hydrocarbon reservoirs. The shape and internal structure of the Niger Delta are also controlled by fracture zones along oceanic crust. The Niger Delta sits at the southern end of Benue trough, corresponding to a failed arm of rift triple junctions (Lehner and De Ruiter, 1977). Figure 1 is the map of Niger delta region of Nigeria showing the location and geology of the study area.

MATERIALS AND METHODS

The goal of gravity survey is to locate and describe subsurface structures from the gravity effects caused by their anomalous densities (Lowrie, 2007; Telford et al., 1990). The variations in acceleration due to earth's gravity are caused by variations in subsurface geology. The aerogravity data was acquired by Nigerian Geological Survey Agency (NGSA). The materials used for this study include four gravity sheets of Olobirin (sheet 327), Degema (sheet 328), Patani (sheet 319) and Ahoda (sheet 320). The data was then transformed to an equally spaced two dimension (2D) grid using the minimum curvature method (Briggs, 1974; Webring, 1981), which fits a minimum curvature surface to data points. This was achieved using the RANGRID GX of the Oasis Montaj^{TM} software. The gridded data helps in producing the Bouguer gravity map. The gridded sheets were digitally merged into a composite aerogravity map which preserved the sanctity of the original maps.

The qualitative interpretation was done to map subsurface structures such as intrusives which may be responsible for the anomalies. This involves the use of grids on which the anomalous values at different stations are plotted and at which contours are drawn at suitable intervals. Then, the quantitative interpretation was done to have the estimates of depths and dimensions of sources of anomalies. The techniques adopted in this study include: source parameter imaging (SPI), Euler deconvolution, forward and inverse modeling (Biswas et al., 2017; Biswas, 2016, 2015).

The source parameter imaging is a technique using an extension of the complex analytical signal to estimate potential field depths (Thurston and Smith, 1997; Nwosu, 2014). This technique is a
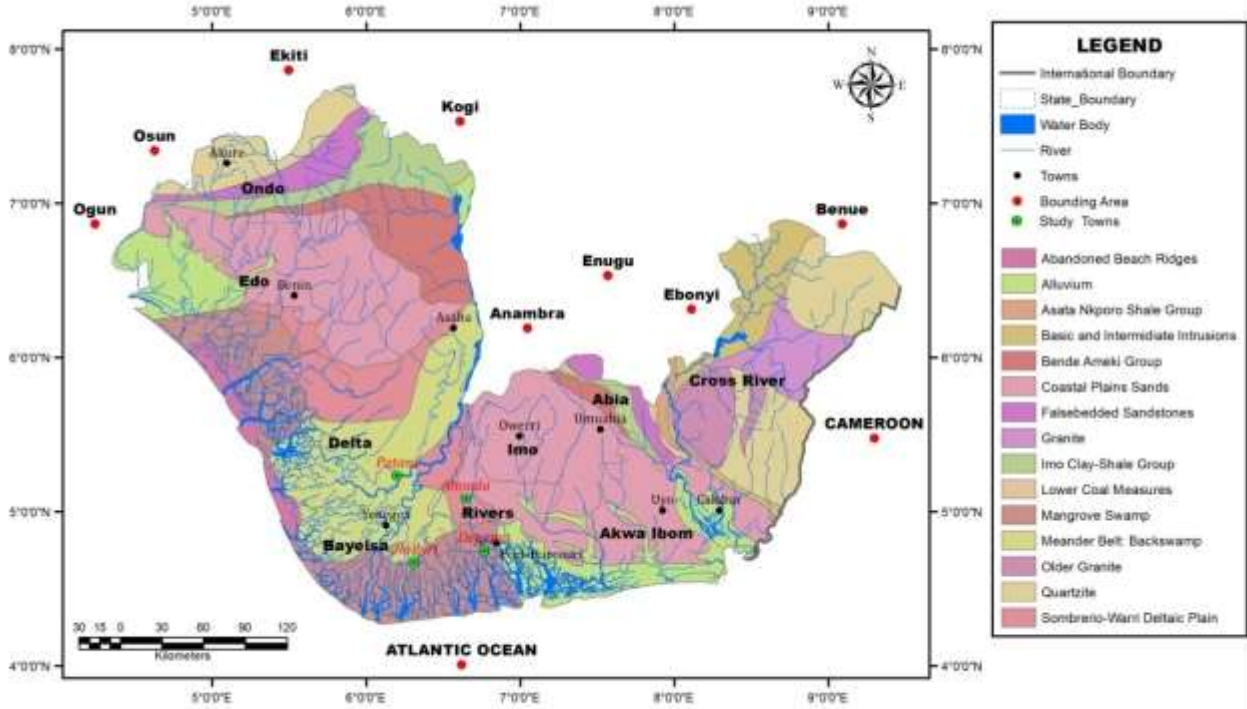
Figure 1. Map showing the location and geology of the study area.

profile or grid-based method for estimating potential source depths and for some source geometries, the dip and density contrast. The method utilizes the relationship between source depth and the local wave number (K) of the observed field, which can be calculated for any point within a grid of data via horizontal and vertical gradients (Thurston and Smith, 1997). The SPI method requires first and second order derivatives and is thus susceptible to both noise in the data and interference effects (Nwosu, 2014). The analytic signal $A_1(x, z)$ is defined by Nabighian (1972) as:

$$A_1(x,z) = \frac{\partial M(x,z)}{\partial x} - j\frac{\partial M(x,z)}{\partial z} \tag{1}$$

where M(x, z) is the magnitude of the anomalous potential field, j is the imaginary number, and z and x are Cartesian coordinates for the vertical direction and the horizontal direction perpendicular to strike, respectively. According to Nabighian (1972), the horizontal and vertical derivatives comprising the real and imaginary parts of the 2D analytical signal are related:

$$\frac{\partial M(x,z)}{\partial x} \Longleftrightarrow -j\frac{\partial M(x,z)}{\partial z} \tag{2}$$

where $\Longleftrightarrow$ denotes a Hilberts transform pair. The local wavenumber K_1 is defined by Thurston and Smith (1997) to be:

$$K_1 = \frac{\partial}{\partial x}\tan^{-1}\left[\frac{\partial M}{\partial z}\Big/\frac{\partial M}{\partial x}\right] \tag{3}$$

Thus, the analytic signal could be defined based on second-order derivatives, $A_2(x, z)$, where

$$A_2(x,z) = \frac{\partial^2 M(x,z)}{\partial z\,\partial x} - j\frac{\partial^2 M(x,z)}{\partial^2 z} \tag{4}$$

This gives rise to a second-order local wave number K_2, where

$$K_2 = \frac{\partial}{\partial x}\tan^{-1}\left[\frac{\partial^2 M}{\partial^2 z}\Big/\frac{\partial^2 M}{\partial z\,\partial x}\right] \tag{5}$$

The first- and second-order local wave numbers are used to determine the most appropriate model and a depth estimate independent of any assumptions about a model (Salako, 2014).

The Euler Deconvolution produces map that show the locations and corresponding depths of the geologic sources observed in a two dimensional grid. The standard Euler 3D method is based on Euler's homogeneity equation, an equation that relates the potential field and its gradient components to the location of the source, with the degree of homogeneity η which may be interpreted as a structural index, SI (Thompson, 1982). The SI is an exponential factor corresponding to the rate at which the field falls off with distance, for a source of a given geometry. The Standard 3D form of Euler's equation (Reid et al., 1990) can be defined as:

$$x\frac{\partial T}{\partial x} + y\frac{\partial T}{\partial y} + z\frac{\partial T}{\partial z} + \eta T = x_0\frac{\partial T}{\partial x} + y_0\frac{\partial T}{\partial y} + z_0\frac{\partial T}{\partial z} + \eta b \tag{6}$$

where x, y, and z are the coordinates of a measuring point; x_0, y_0, and z_0 are the coordinates of the source location whose total field is detected at x, y, and z; b is a base level; η is structural index (SI) and T is potential field. The value of the SI depends on the type of source body under investigation (Whitehead and Musselman, 2005). For example $\eta = 0$ for a horizontal contact with infinite dimensions, $\eta = 0.5$ for a vertical contact, $\eta = 1$ for top of a vertical
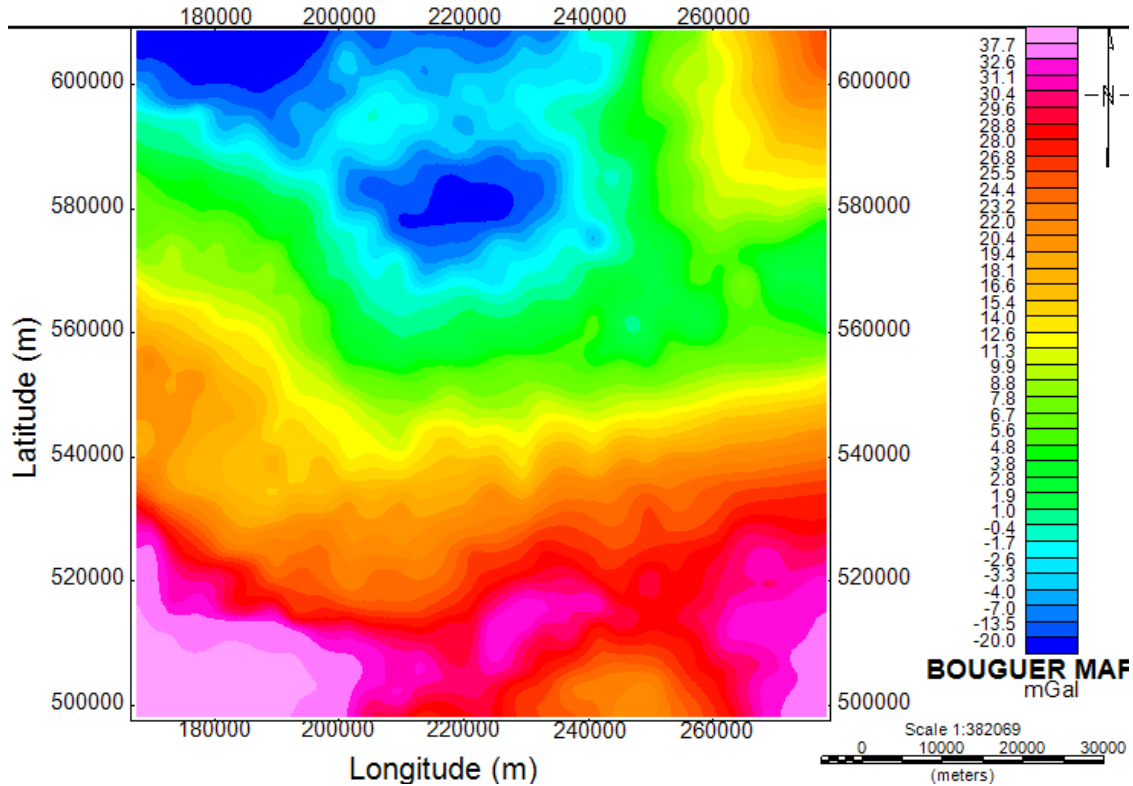
Figure 2. Bouguer gravity map of the study area.

dyke or the edge of a sill, $\eta = 2$ for the centre of a horizontal or vertical cylinder and $\eta = 3$ for the centre of a magnetic sphere or dipole (Thompson, 1982; Reid et al., 1990; Moghaddam et al., 2015).

In modeling, the PotentQ 3D tool of the Oasis montaj[TM] is used; it involves making numerical estimates of the depth and dimensions of the sources of anomalies. The forward modeling is a trial and error method; in which the shape, position and physical properties of the models are adjusted in order to obtain a good fit between the calculated field and the observed field data. The inverse modeling involves a mathematical process that automatically adjusts the model parameters so as to improve the fit between the calculated field and the observed field.

RESULTS AND DISCUSSION

The result from the interpreted data shows that Bouguer anomaly of the study area varies from -20.0 to 37.7 mGal (Figure 2). These values indicate the presence of coastal-oceanic regions where the Bouguer gravity values drops to zero as we move close to the coast (Robinson and Coruh, 1988). The regions of gravity high correspond to region with high density contrast beneath the surface and gravity low corresponds to region of low density contrast. The residual Bouguer anomaly varies from -19.6l to 25.7 mGal. The southern part of the study area has high density contrast beneath the subsurface and decreases

towards the northern part (Figure 3). The regional Bouguer anomaly varies from 11.7 to 14.4 mGal (Figure 4).

Figure 5 is the horizontal derivative computed from the residual Bouguer gravity grid using Oasis montaj[TM] software. The horizontal derivative map (Figure 5) shows more exact location for faults.

Figure 6 is the aerogravity SPI map showing the variation of depths to anomalous gravity bodies computed using the first vertical derivatives and horizontal gradient. The negative depth values depicts the depths of buried gravity bodies, which may be deep seated basement rocks or near surface intrusive. The pink colour generally indicates areas occupied by shallow gravity bodies, while the blue colour depicts areas of deep lying gravity bodies. The SPI depth result varies from -539.7 m (shallow gravity anomalous bodies) to -4276.7 m (deep lying gravity anomalous bodies). The high depths indicate thick sediment which is suitable for hydrocarbon accumulation (Wright et al., 1985, Obiora et al., 2016).

The Euler depths were estimated using vertical derivatives in three dimensions (x, y, and z), vertical derivatives enhance shallow gravity bodies. Hence, depths of shallow gravity anomalies for different structural index are displayed by Euler method. Different structural
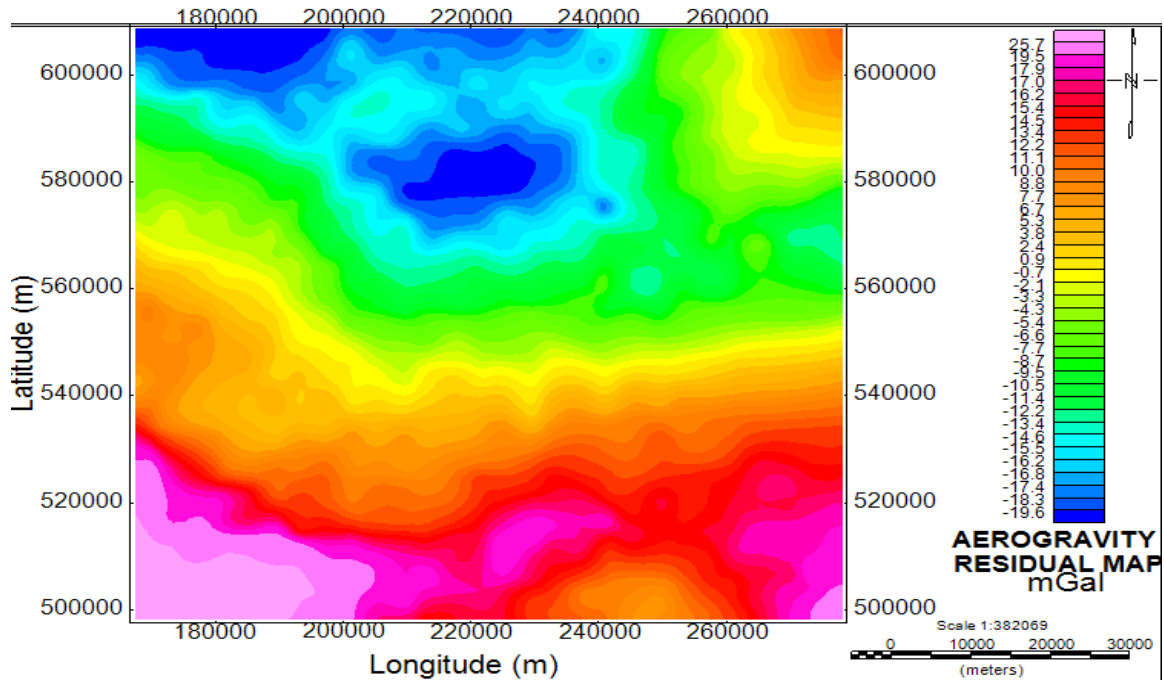
Figure 3. Residual gravity map of the study area.
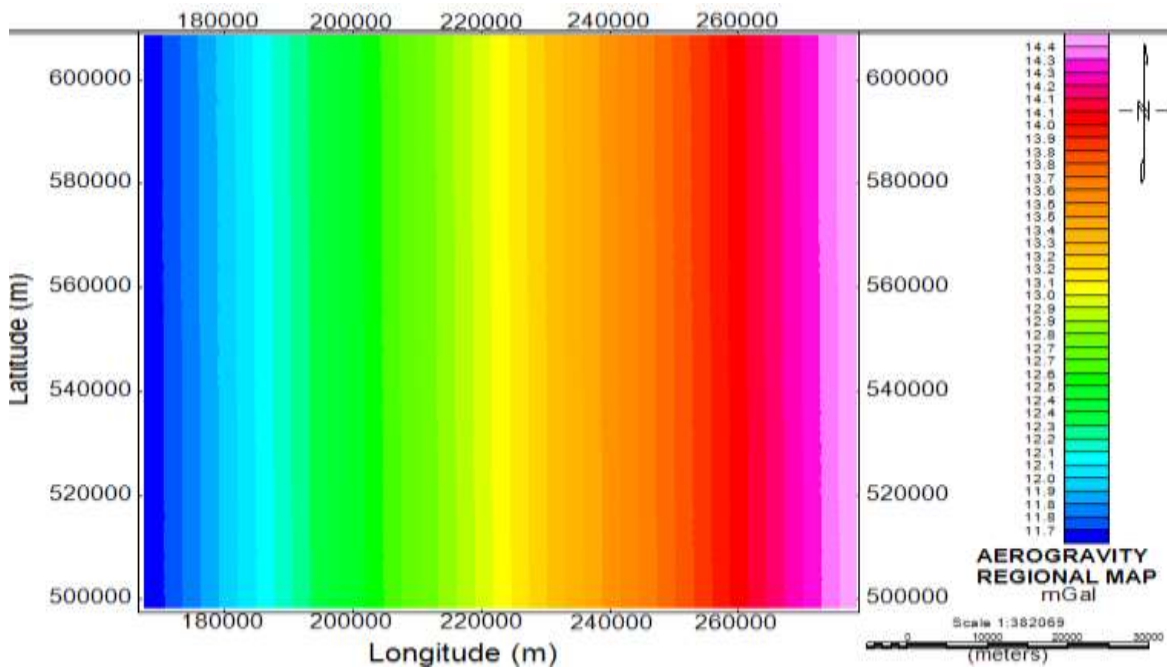
Figure 4. Regional gravity intensity map of the study area.

index numbers were tried on the data but it was found that the index number 0, 1 and 2 were the best for the data as it reflected the geological information of the area. Three Euler deconvolution maps were generated as shown in Figure 7a, b and c for the aerogravity data. The pink colour indicates shallow gravity bodies, while the blue colour indicates deep lying gravity bodies. The Euler depth result ranges from -1518.1 to 1355.5, -3283.2 to

Figure 5. Aerogravity horizontal derivative map of the study area.

Figure 6. Source parameter image (SPI) map of the study area.

2384.0 m, and -5011.4 to 2426.0 m for structural index of 0, 1, and 2, respectively. The results of Euler 3D depths are summarized in Table 1.
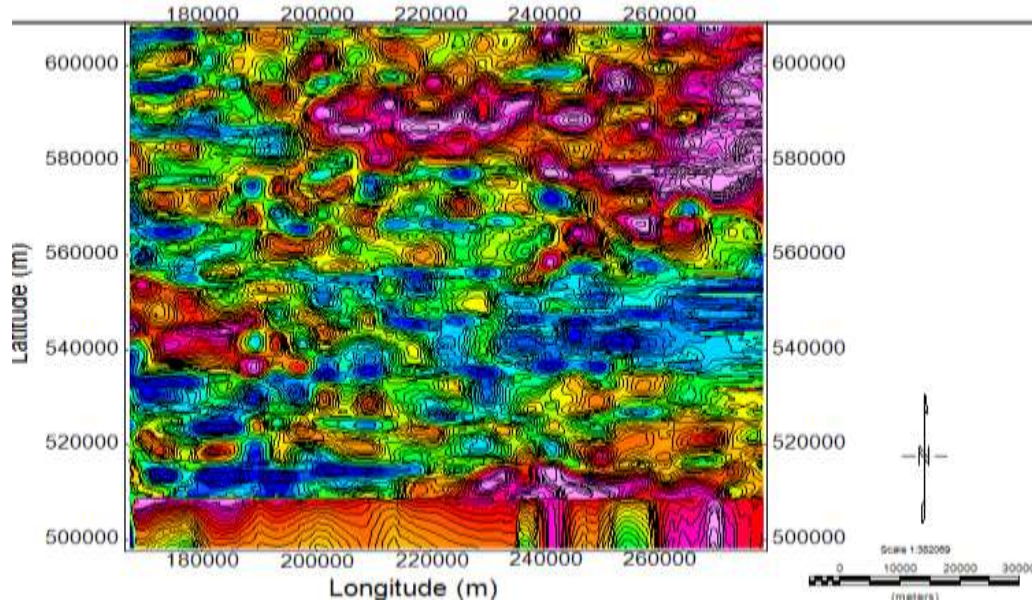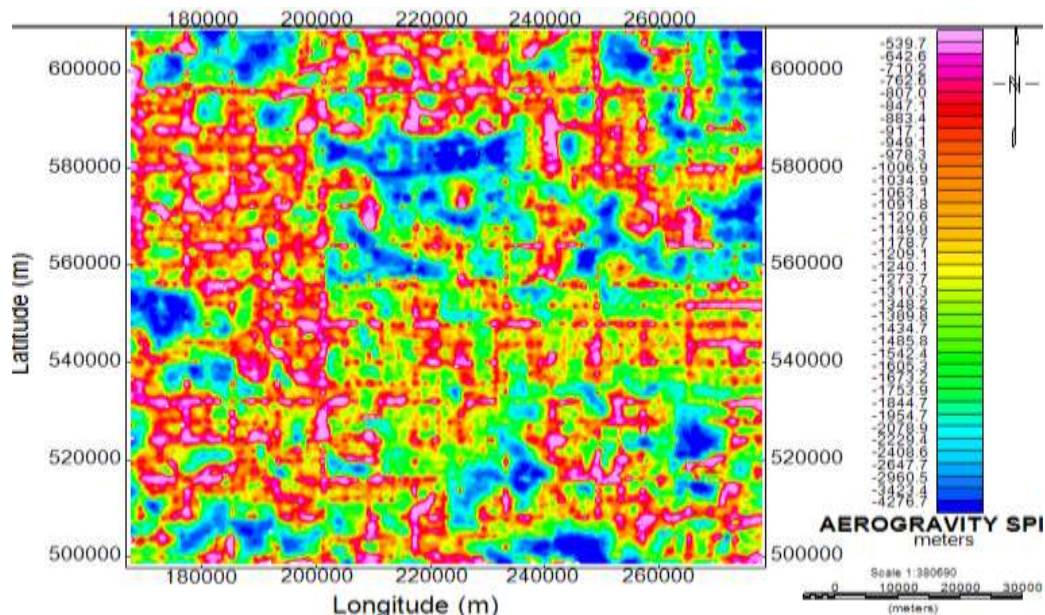
Five profiles were taken on the residual Bouguer grid (Figure 8) and modeled in order to show the distribution of causative bodies within the selected area. Each profile produced a degree of strike, dip and plunge where the observed values matched well with the calculated values. The blue curves represent the observed field values while the red curves represent the calculated field values. The forward modeling being a trial and error method, the shape, position and physical properties of the model were adjusted in order to obtain a good correlation between the calculated field and the observed field data. Using PotentQ 3D tool of the Oasis montaj™ software, the field of the model was calculated. The root mean square (RMS) difference between the observed and calculated field values were attempted to be minimized by the
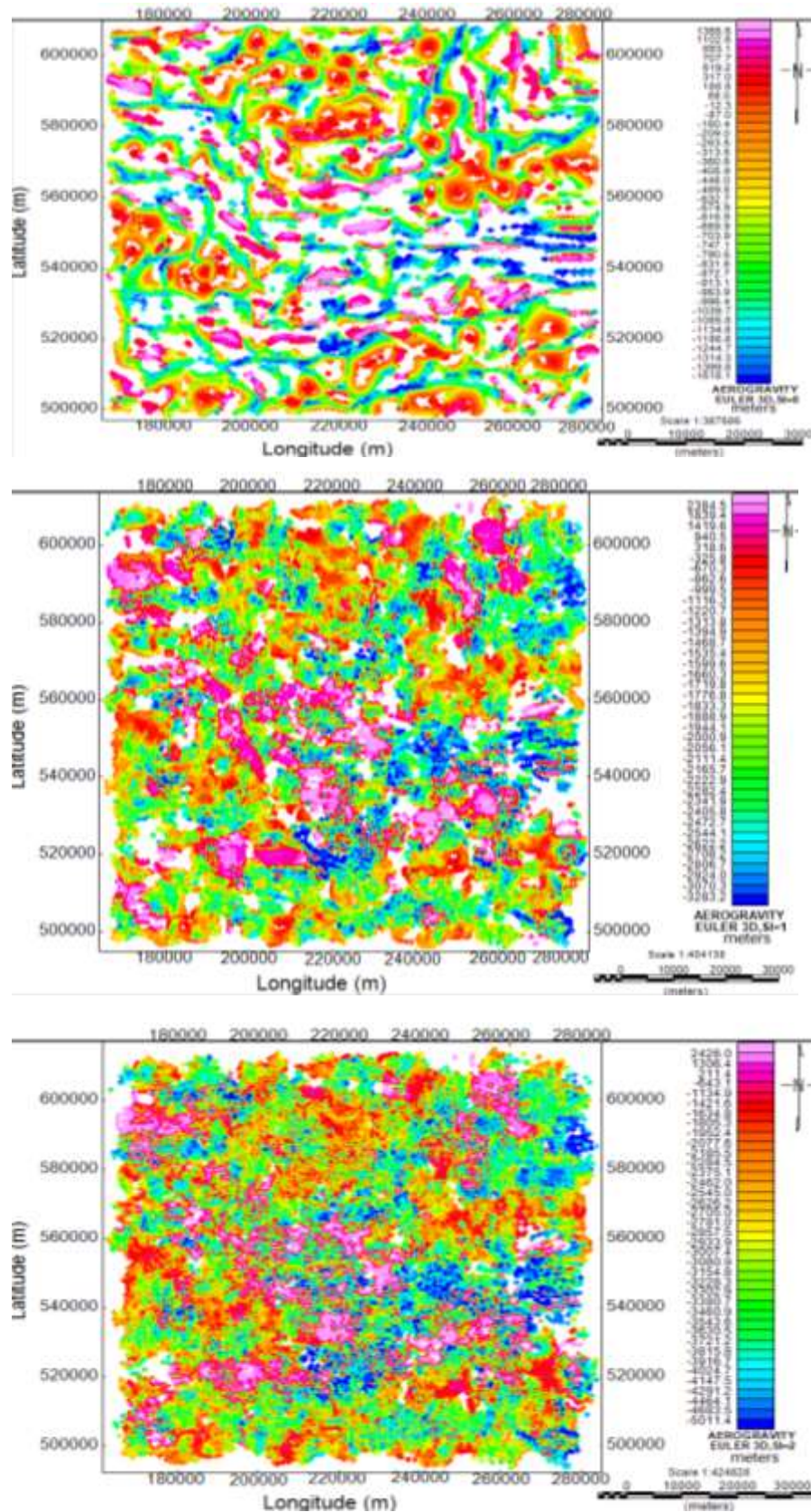
Figure 7. (a) Aerogravity Euler 3D depth map, SI=0; (b) Aerogravity Euler 3D depth map, SI=1; (c): Aerogravity Euler 3D depth map, SI=2.

Table 1. Depth estimates for Euler-3D Deconvolution.

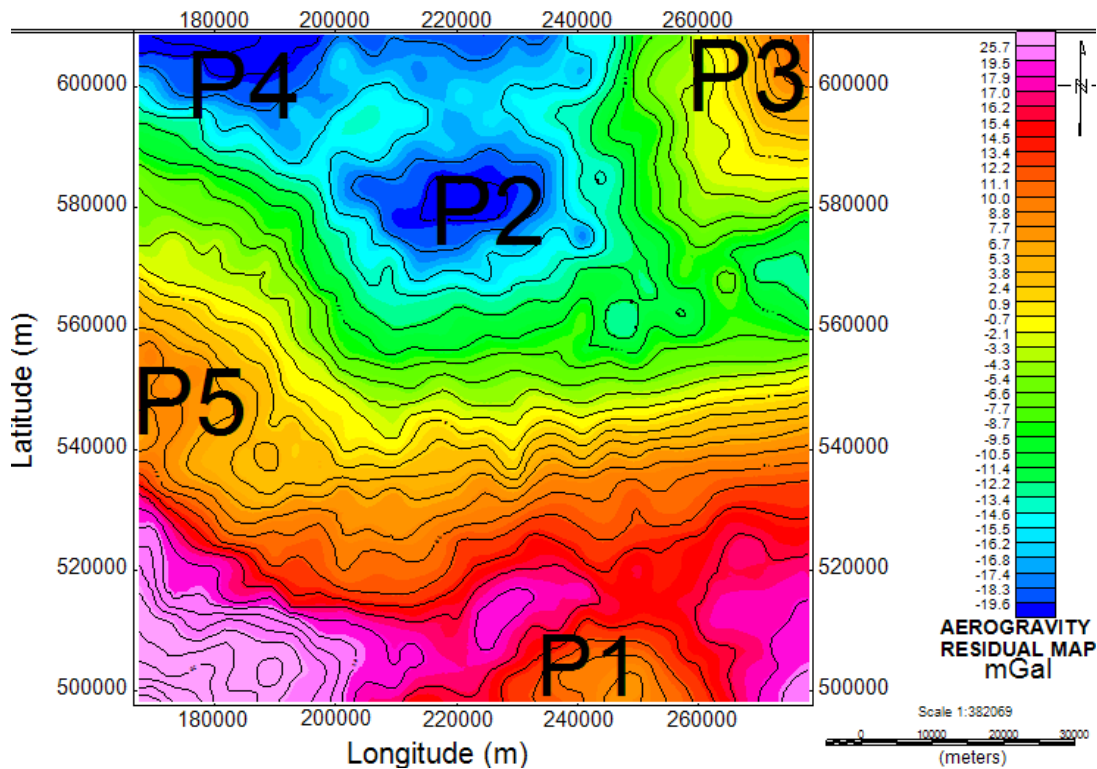| Structural index, SI	Depth ranges (m) Bouguer gravity data
0	1355.5 to -1518.1
1	2384.5 to -3283.2
2	2426.0 to -5011.4

Figure 8. Aerogravity Residual contour map.

inversion algorithm. At the end of the inversion, the RMS value was displayed. The RMS value decreased as the fit between the observed and calculated field continues to improve, until a reasonable inversion result was achieved. Less than 5% of root mean square value was set as the error margin. The modeled profiles are shown in Figure 9a to e and the results of the forward and inverse modeling are summarized in Table 2. The result from the forward and inverse modeling analysis of the aerogravity data shows that the density values obtained from the modeled profiles 1, 2, 3, 4 and 5 are 1.820, 2.410, 0.720, 2.310 and 2.100 g/cm^3, respectively, with respective depths of 3872, 4228, 4880, 3560 and 2527 m. These density values indicate the presence of minerals like petroleum, clay, gypsum, kaolinite and rock bearing minerals like shale, limestone and marble in the study area (Thompson and Oldfield, 1986; Telford et al., 1990; Hunt et al., 1995). The observed depths indicate thick sediments that confirms the feasibility for

hydrocarbon accumulation in the area.

Conclusion

Aerogravity data covering Olobirin (sheet 327), Degema (sheet 328), Patani (sheet 319) and Ahoda (sheet 320) in Niger Delta region of Nigeria were interpreted. Source parameter imaging (SPI), Euler deconvolution and forward and inverse modeling techniques were employed in quantitative interpretation with the aim of determining depth/thickness of the sedimentary basin, basement topography, density contrasts, and types of mineralization prevalent in the area.

The Bouguer anomaly of the study area varies from -20.0 to 37.7 mGal while the residual Bouguer anomaly of the study area varies from -19.6 to 25.7 mGal. These values are indicative of coastal-oceanic regions where the Bouguer gravity values drop to zero as we move
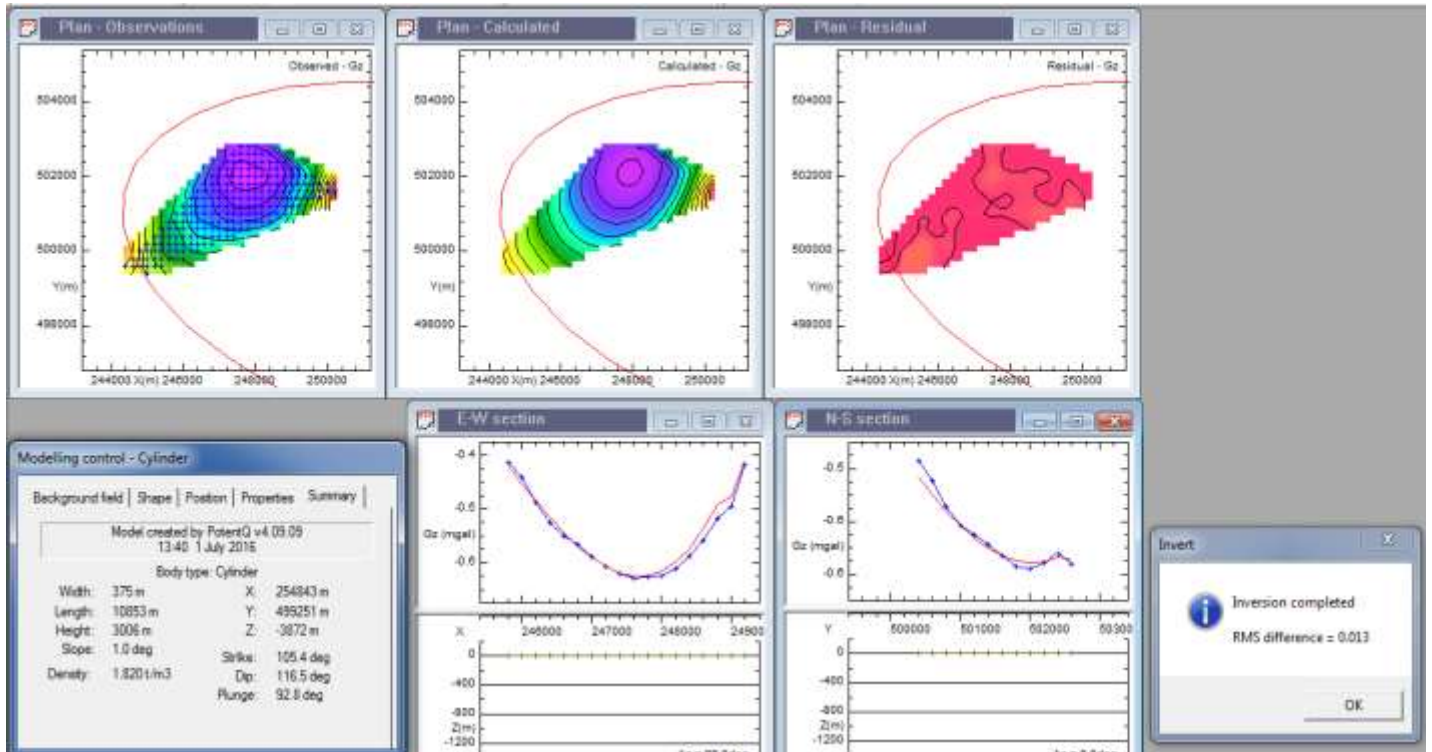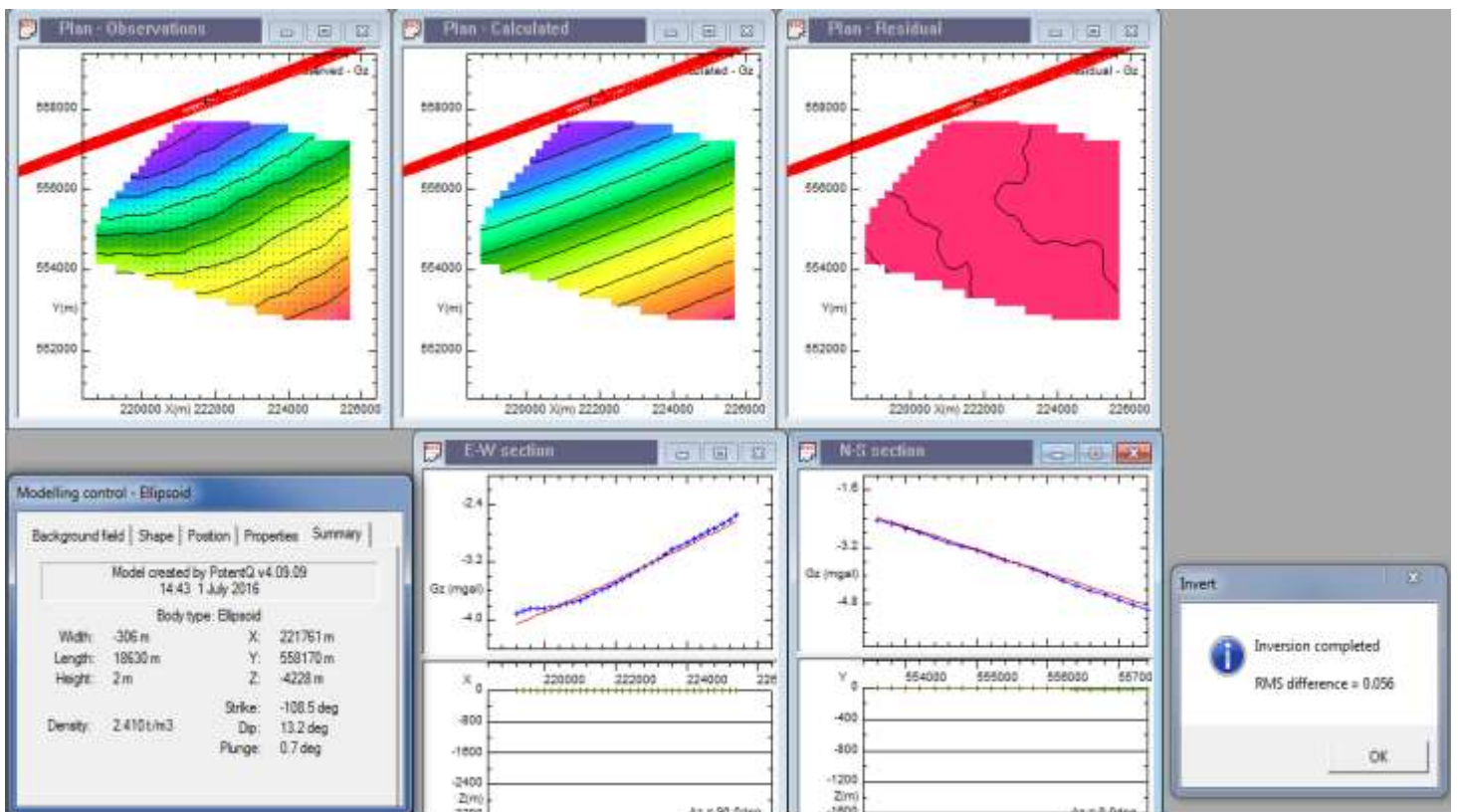
Figure 9a. Profile 1 (P1) modeled.
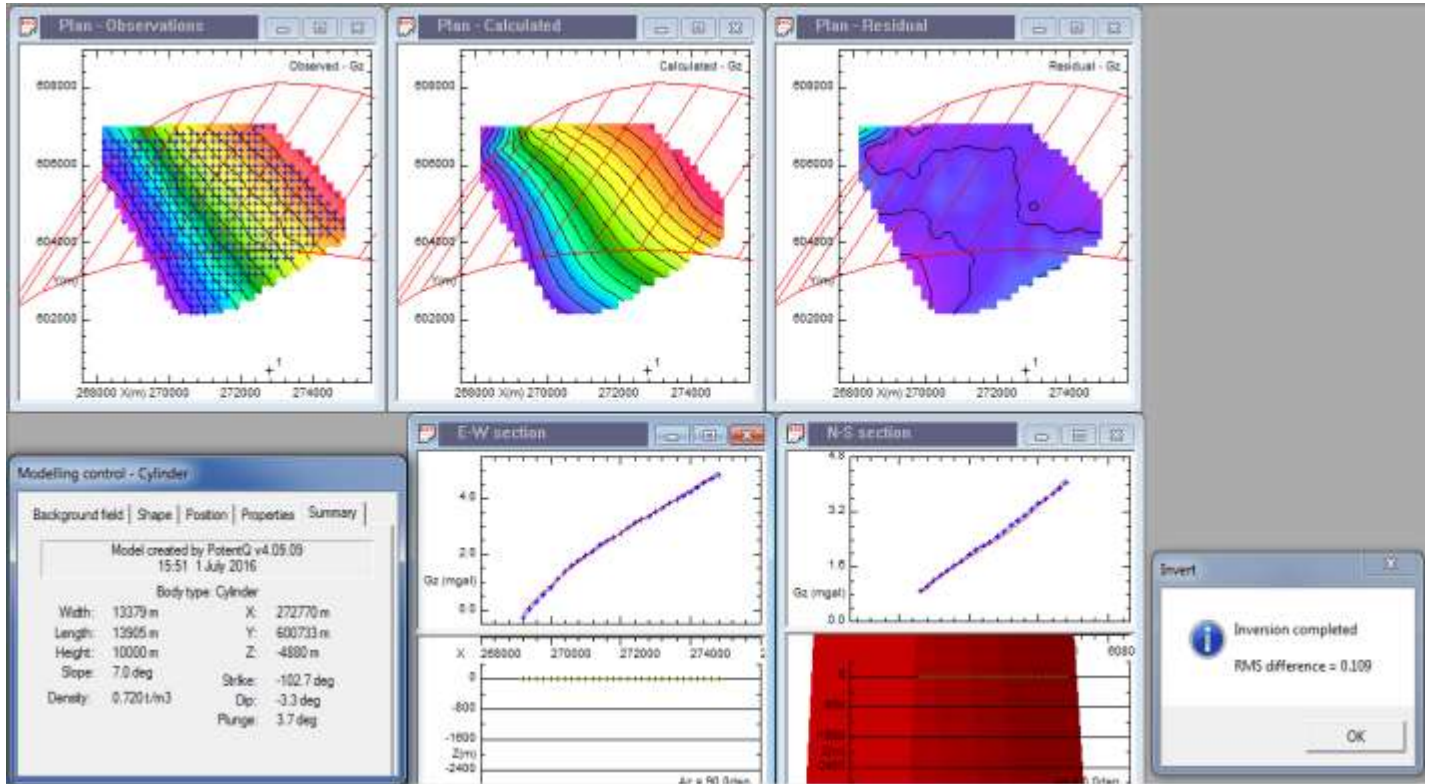

Figure 9b. Profile 2 (P2) modeled.

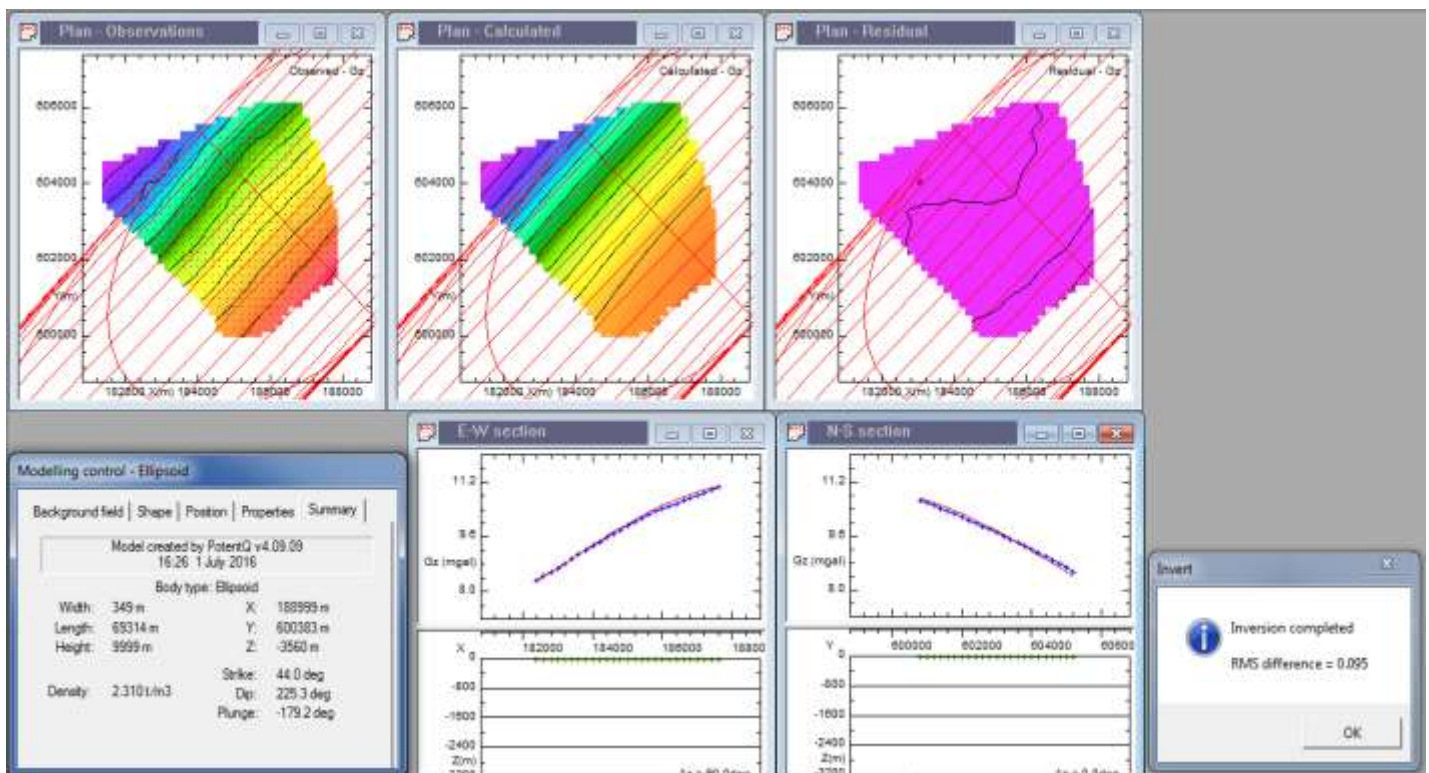**Figure 9c.** Profile 3 (P3) modeled.

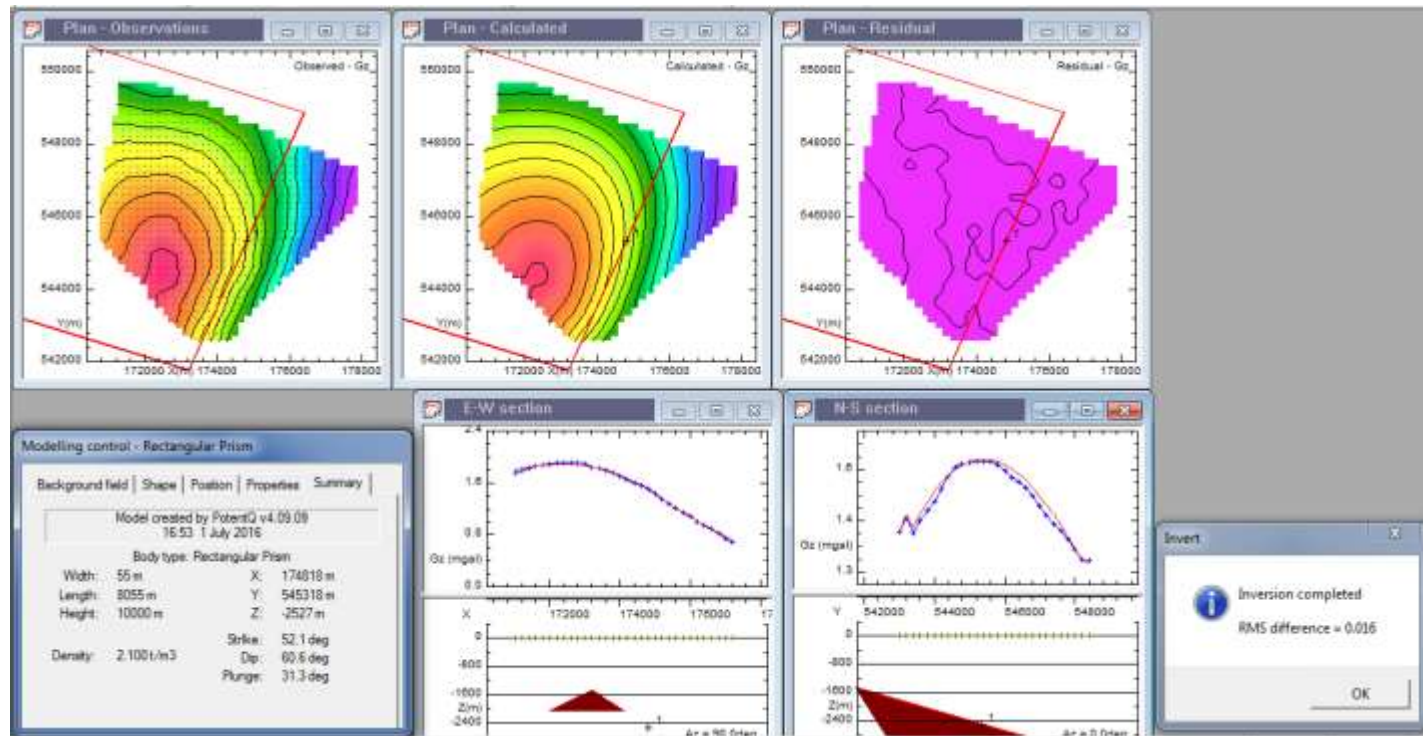**Figure 9d.** Profile 4 (P4) modeled.

Figure 9e. Profile 5 (P5) modeled.

Table 2. Summary of aerogravity forward and inverse modeling results.

Model	Model shape	X (m)	Y (m)	Depth to anomalous body (m)	Plunge (deg)	Dip (deg)	Strike (deg)	Density value (g/cm^3)	Possible cause of anomaly
P6	Cylinder	254843	499251	3872	92.8	116.5	105.4	1.820	Shale
P7	Ellipsoid	221761	558170	4228	0.7	-13.2	-108.5	2.410	Gypsum
P8	Cylinder	272770	600733	4880	3.7	-3.3	-102.7	0.720	Petroleum
P9	Ellipsoid	188999	600383	3560	-179.2	225.3	44.0	2.310	Kaolinite
P10	Rectangular prism	174818	545318	2527	31.3	60.6	52.1	2.100	Limestone

close to the coast and also show the heterogeneous nature of the study area. The contour maps reveal regions with gravity high and low which correspond to regions of high and low density contrast, respectively. The source parameter image (SPI) grid indicates the different density contrast and magnetic susceptibility within the area. The SPI depth result for the aerogravity data ranges from -539.7 to -4276.7 m.

The windowed Euler-3D for the Bouguer gravity results show that for structural index of one, the depth range is between 1355.5 and -1518.1 m; for structural index of two, the depth range is between 2384.5 and -3283.2 m, while for structural index of three, it is between 2426.0 and -5011.4 m. The results from the forward and inverse modeling analysis of the aerogravity data show that the density values obtained from the modeled profiles 6, 7, 8,

9 and 10 are 1.820, 2.410, 0.720, 2.310 and 2.100 g/cm^3, respectively, with respective depths of 3872, 4228, 4880, 3560 and 2527 m. The results indicated that the estimated sedimentary thickness and variation of the geological structures that makes the region is suitable for hydrocarbon and other minerals accumulation in the study area.

CONFLICT OF INTERESTS

The authors have not declared any conflict of interests.

REFERENCES

Adedapo JO, Ikpokonte AE, Kurowska E, Schoeneich K (2014). An

Estimate of Oil Window in Nigeria Niger Delta Basin from Recent Studies. Am. Int. J. Cont. Res. 4(9):114-121.

Agunleti YS, Saua SL (2015). Geochemical Studies and Exploration potential of the Oolitic-Pisolitic Ironstone deposits of Agbaja Formation Southern Bida Basin, North-central Nigeria. Int. J. Innov. Sci. Eng. Tech. 2(5):527-528.

Biswas A (2017a). A Review on Modeling, Inversion and Interpretation of Self-Potential in Mineral Exploration and Tracing Paleo-Shear Zones. Ore Geol. Rev. 91:21-56.

Biswas A (2017b). Inversion of source parameters from magnetic anomalies for mineral /ore deposits exploration using global optimization technique and analysis of uncertainty. Nat. Res. Res. DOI: 10.1007/s11053-017-9339-2.

Biswas A, Parija MP, Kumar S (2017). Global nonlinear optimization for the interpretation of source parameters from total gradient of gravity and magnetic anomalies caused by thin dyke. Ann. Geophys. 60(2):G0218, 1-17.

Biswas A, Sharma SP (2016). Integrated geophysical studies to elicit the structure associated with Uranium mineralization around South Purulia Shear Zone, India: A Review. Ore Geol. Rev. 72:1307-1326.

Biswas A (2015). Interpretation of residual gravity anomaly caused by a simple shaped body using very fast simulated annealing global optimization. Geosci. Front. 6(6):875-893.

Biswas A, Sharma SP (2015). Interpretation of self-potential anomaly over idealized body and analysis of ambiguity using very fast simulated annealing global optimization. Near Surf. Geophys. 13(2):179-195.

Biswas A, Sharma SP (2014a). Optimization of Self-Potential interpretation of 2-D inclined sheet-type structures based on Very Fast Simulated Annealing and analysis of ambiguity. J. Appl. Geophys. 105:235–247.

Biswas A, Sharma SP (2014b). Resolution of multiple sheet-type structures in self-potential measurement. J. Earth Syst. Sci. 123(4): 809–825.

Biswas A, Mandal A, Sharma SP, Mohanty WK (2014a). Delineation of subsurface structure using self-potential, gravity and resistivity surveys from South Purulia Shear Zone, India: Implication to uranium mineralization. Interpretation 2(2):T103-T110.

Biswas A, Mandal A, Sharma SP, Mohanty WK (2014b). Integrating apparent conductance in resistivity sounding to constrain 2D Gravity modeling for subsurface structure associated with uranium mineralization across South Purulia Shear Zone. Int. J. Geo. pp. 1-8.

Biswas A (2016). Interpretation of gravity and magnetic anomaly over thin sheet-type structure using very fast simulated annealing global optimization technique. Model. Earth Syst. Environ. 2(1):30.

Briggs IC (1974). Machine contouring using minimum curvature. Geophysics 39(1):39-48.

Doust H, Omatsola E (1990). Niger Delta. In *Divergent Passive Margin Basins.* JD. Edwards and PA Santogrossi (eds). American Association of Petroleum Geologists. Memoir 48:201-238.

Ezekiel JC, Onu NN, Akaolisa CZ, Opara AI (2013). Preliminary Interpretation of gravity mapping over the Njaba sub-basin of Southeastern Nigeria. An implication to petroleum potential. J. Geol. Min. Res. 5(3):75-87.

Evamy BD, Harebourne J, Kamerling P, Knaap WA, Molloy FA, Rowlands PH (1978). Hydocarbon habitat of Tertiary Niger Delta. Bull. Am. Assoc. Pet. Geol. 62(1):1-39.

Hosper J (1965). Gravity field and structure of the Niger Delta, Nigeria, West Africa. Geol. Soc. Am. Bull. 76:407-4222.

Hunt CP, Moskowitz BM, Banerjee SK (1995). Magnetic properties of rocks and minerals, in Ahrens, T.J., ed., Rock Physics and Phase Relations: A Handbook of Physical Constants. Am. Geophys. Union 3:189–204.

Johnson EAE (1998). Gravity and magnetic analyses can address various petroleum issues. Geologicapplications of Gravity and Magnetic: case Histories. In Gibson I, Millegan PS (Eds.). SEGGeophysical Reference No.8 and AAPG Studies in Geology 43:7-8. Tulsa, United States.

Lehner D, De Ruiter PAC (1977). Structural history of Atlantic margin of Africa. AAPG Bull. 61:961-981.

Lowrie W (2007). Fundamentals of Geophysics. Cambridge University Press, London.

Mandal A, Mohanty WK, Sharma SP, Biswas A, Sen J, Bhatt AK (2015). Geophysical signatures of uranium mineralization and its subsurface validation at Beldih, Purulia District, West Bengal, India: A case study. Geophys. Prospect. 63:713-726.

Mandal A, Biswas A, Mittal S, Mohanty WK, Sharma SP, Sengupta D, Sen J, Bhatt AK (2013). Geophysical anomalies associated with uranium mineralization from Beldih mine, South Purulia Shear Zone, India. J. Geol. Soc. Ind. 82(6):601-606.

Mbah D, Obiora DN, Oha AI, Terhemba BS, Ossai CO, Igwe EA (2017). Investigation of possible cause of gravity anomalies in parts of the Niger Delta basin, Nigeria. Int. J. Phys. Sci. 12(9):103-117.

Merki PI (1972). Structural Geology of the Cenozoic Niger Delta. Afr. Geol. University of Ibadan Press, pp. 251-260.

Mickus K (2004). The gravity method in engineering and environmental applications, In: Geophysics 2003: Federal Highway Administration and Florida Department of Transportation special publication.

Moghaddam MM, Sabseparvar M, Mirzaei S, Heydarian N (2015). Interpretation of Aeromagnetic Data to Locate Buried Faults in North of Zanjan Province, Iran. J. Geophys. Rem. Sens. 4:143.

Nabighian MN (1972). The analytic signal of two dimensional magnetic bodies with polygonal cross-section: Its properties and use for automated anomaly interpretation. Geophysics 37(3):507-517.

Nwosu OB (2014). Determination of Magnetic Basement Depth over Parts of Middle Benue Trough by Source Parameter Imaging (SPI) Technique Using HRAM. Int. J. Sci. Tech. Res. 3(1):262.

Obiora DN, Ossai MN, Okeke FN, Oha AI (2016). Interpretation of airborne geophysical data of Nsukka area, Southeastern Nigeria. J. Geol. Soc. Ind. 88:654-667.

Okiwelu AA, ofrey-Kulo O, Ude IA (2013). Interpretation of regional magnetic data offshore Niger Delta reveals relationship between deep basement architecture and hydrocarbon target. Earth Sci. Res. 2(1):13-32.

Reid AB, Allsop JM, Grauser H, Millet AJ, Somerton IN (1990). Magnetic interpretation in three dimensions using Euler deconvolution. Geophysics 55(1):80-91.

Robinson ES. Coruh C (1988.) Basic exploration Geophysics. New York.

Salako KA (2014). Depth to Basement Determination Using Source Parameter Imaging (SPI) of Aeromagnetic Data: An Application to Upper Benue Trough and Borno Basin, Northeast, Nigeria. Acad. Res. Int. 5(3):74-86.

Singh A, Biswas A (2016). Application of global particle swarm optimization for inversion of residual gravity anomalies over geological bodies with idealized geometries. Nat. Res. Res. 25(3):297-314.

Sharma SP, Biswas A (2013). Interpretation of self-potential anomaly over 2D inclined structure using very fast simulated annealing global optimization–An insight about ambiguity. Geophysics 78(3):WB3–15.

Telford WM, Geldart LP, Sheeriff RE (1990). Applied geophysics (2nd edition). Cambridge University press, Cambridge.

Thompson DT (1982). A new technique for making computer-assisted depth estimates from magnetic data. Geophysics 47(1):31-37.

Thompson R, Oldfield F (1986). Environmental Magnetism: London, Allen and Unwin, 227.

Thurston JB, Smith RS (1997). Automatic conversion of magnetic data to depth, dip, and susceptibility contrast using the SPI[TM] method. Geophysics 62(3):807-813.

Tuttle MLW, Charpentier RR, Brownfield ME (1999). The Niger Delta petroleum system: Niger Delta province, Nigeria, Cameroun and Equatorial Guinea, Africa, U. S. Geological Survey Open-fileReport-99-50-H, 31P.

Webring M (1981). MINC: a gridding program based on minimum curvature. *U.S. Geological Survey* 81-1224:43.

Whitehead N, Musselman C (2005). Montaj[TM]Grav/Mag interpretation: Processing, analysis and visualization system for 3D inversion of potential field data for Oasis montaj v6.1. Geosoft Inc. ON, Canada.

Wright JB, Hastings D, Jones WB, Williams HR (1985.) Geology and Mineral Resources of West Africa. George Allen and Unwind publ. London.

Related Journals:

African Journal of
Pure and Applied Chemistry

Journal of
**Environmental Chemistry
and Ecotoxicology**

Journal of
Geology and Mining Research

Journal of
**Internet and
Information Systems**

Journal of
**Oceanography and
Marine Science**

Journal of
**Petroleum Technology
and Alternative Fuels**

Journal of
**Agricultural
Biotechnology and
Sustainable Development**

International Journal of
Physical Sciences

Scientific Research and Essays

academicJournals

www.academicjournals.org